AFRL-AFOSR-VA-TR-2020-0148

Adaptable Compressed Jaumann Absorber for Harsh and Dynamic EM Enviroments

Jae Oh
SYRACUSE UNIVERSITY

08/18/2020
Final Report

Air Force Research Laboratory
AF Office Of Scientific Research (AFOSR)/ RTB1
Arlington, Virginia 22203
Air Force Materiel Command

DISTRIBUTION A: Distribution approved for public release.

REPORT DOCUMENTATION PAGE

Form Approved
OMB No. 0704-0188

1. REPORT DATE *(DD-MM-YYYY)*	2. REPORT TYPE	3. DATES COVERED *(From - To)*
24-08-2020	Final Performance	01 Feb 2017 to 30 Jun 2020

4. TITLE AND SUBTITLE
Adaptable Compressed Jaumann Absorber for Harsh and Dynamic Electromagnetic Environments

5a. CONTRACT NUMBER

5b. GRANT NUMBER
FA9550-17-1-0111

5c. PROGRAM ELEMENT NUMBER
61102F

6. AUTHOR(S)
Jae Oh, Jun Choi

5d. PROJECT NUMBER

5e. TASK NUMBER

5f. WORK UNIT NUMBER

7. PERFORMING ORGANIZATION NAME(S) AND ADDRESS(ES)
SYRACUSE UNIVERSITY
CONTROLLERS OFFICE SKYTOP OFFICE BLD
SYRACUSE, NY 13244 US

8. PERFORMING ORGANIZATION REPORT NUMBER

9. SPONSORING/MONITORING AGENCY NAME(S) AND ADDRESS(ES)
AF Office of Scientific Research
875 N. Randolph St. Room 3112
Arlington, VA 22203

10. SPONSOR/MONITOR'S ACRONYM(S)
AFRL/AFOSR RTB1

11. SPONSOR/MONITOR'S REPORT NUMBER(S)
AFRL-AFOSR-VA-TR-2020-0148

12. DISTRIBUTION/AVAILABILITY STATEMENT
A DISTRIBUTION UNLIMITED: PB Public Release

13. SUPPLEMENTARY NOTES

14. ABSTRACT
The need for tunable, low-profile, light-weight, and high-power handling absorbers has increased significantly as aerospace applications demand reliable radio-frequency/microwave radar cross section (RCS) reduction devices that can rapidly adapt to harsh and dynamic electromagnetic (EM) environments while enabling a more agile flight maneuverability. However, the current tunable absorber technologies have critical limitations, particularly due to tuning elements such as PIN diodes, varactors, MEMS, and liquid crystal polymers that require tradeoffs between tuning range, reliability, linearity, cost, and weight. More importantly, most of these elements become vulnerable when subject to damaging levels of EM radiation from electronic warfare including high-power microwave weapons, radars, and jammers which create the harsh electromagnetic environment in which they need to operate. Aside from these inadequate tuning elements, current methods fail to provide a simple yet comprehensive design synthesis process that can assure stable operation of EM absorbers over broad bandwidth and arbitrary polarizations in a low-profile form factor. In this project, we will investigate generalized synthesis techniques and the feasibility of devising electronically tunable compressed Jaumann absorbers based on plasma electrical properties to address the critical limitations of current techniques. A multiphysics analysis (which requires EM and thermal co-simulation) is performed on a two-pole high power microwave (HPM) absorber under high power excitation. The maximum power handling capability of the device has been numerically predicted and validated experimentally.

15. SUBJECT TERMS
FSS, frequency selective surfaces, Jaumann absorber, plasma shell, metamaterial, metasurface, radar

16. SECURITY CLASSIFICATION OF:

Standard Form 298 (Rev. 8/98)
Prescribed by ANSI Std. Z39.18

a. REPORT	b. ABSTRACT	c. THIS PAGE	17. LIMITATION OF ABSTRACT	18. NUMBER OF PAGES	19a. NAME OF RESPONSIBLE PERSON
Unclassified	Unclassified	Unclassified	UU		MOSES, JULIE
					19b. TELEPHONE NUMBER *(Include area code)* 703-696-9586

No. FA9550-17-1-0111

ADAPTABLE COMPRESSED JAUMANN ABSORBER FOR HARSH AND DYNAMIC ELECTROMAGNETIC ENVIRONMENTS

Material sponsored by the Air Force Office of Scientific Research under AFOSR Award No. FA9550-17-1-0111.

Final Performance Report
Due September 30, 2020

Syracuse University
Center for Science & Technology
Syracuse, NY 13244-4100

No. FA9550-17-1-0111

REPORT DOCUMENTATION PAGE

1. REPORT TYPE	2. DATES COVERED (From - To)
Final Performance Report	February 15, 2017 to June 30, 2020

3. TITLE AND SUBTITLE

Adaptable Compressed Jaumann Absorber for Harsh and Dynamic Electromagnetic Environments

4. AUTHORS

Komlan Payne[1] & Jae Oh[1](e-mail: kopayne@syr.edu, jcoh@syr.edu)

Kevin Xu[2] & Jun H. Choi[2] (e-mail: kxu22@buffalo.edu, junhchoi@buffalo.edu).

5. PERFORMING ORGANIZATION NAMES AND ADDRESSES

[1]Center for Science & Technology; Syracuse University; Syracuse, NY, 13244 USA.

[2]Department of Electrical Engineering; University at Buffalo; Buffalo, NY, 14260 USA.

6. SPONSORING AGENCY NAME AND ADDRESS

Air Force Office of Scientific Research; 875 N. Randolph; Arlington, VA 22203.

7. ABSTRACT

The need for tunable, low-profile, light-weight, and high-power handling absorbers has increased significantly as aerospace applications demand reliable radio-frequency/microwave radar cross section (RCS) reduction devices that can rapidly adapt to harsh and dynamic electromagnetic (EM) environments while enabling a more agile flight maneuverability. However, the current tunable absorber technologies have critical limitations, particularly due to tuning elements such as PIN diodes, varactors, MEMS, and liquid crystal polymers that require tradeoffs between tuning range, reliability, linearity, cost, and weight. More importantly, most of these elements become vulnerable when subject to damaging levels of EM radiation from electronic warfare including high-power microwave weapons, radars, and jammers which create the harsh electromagnetic environment in which they need to operate. Aside from these inadequate tuning elements, current methods fail to provide a simple yet comprehensive design synthesis process that can assure stable operation of EM absorbers over broad bandwidth and arbitrary polarizations in a low-profile form factor. In this project, we will investigate generalized synthesis techniques and the feasibility of devising electronically tunable compressed Jaumann absorbers based on plasma electrical properties to address the critical limitations of current techniques. A multiphysics analysis (which requires EM and thermal co-simulation) is performed on a two-pole high power microwave (HPM) absorber under high power excitation. The maximum power handling capability of the device has been numerically predicted and validated experimentally.

8. SUBJECT TERMS

Electronic protection, frequency selective surface-based absorber, high power microwave, plasma devices, radar cross section, tunable absorber.

Table of Contents

List of Tables

List of Figures

List of Symbols, Abbreviations and Acronyms

AC	alternating current
AFOSR	Air Force Office of Scientific Research
AFRL	air force research laboratory
CAA	circuit analog absorbers
C-band	IEEE microwave band, 4–8 GHz
CW	continuous wave
DC	direct current
DEW	directed energy weapons
DoD	Department of Defense
DUT	device under test
EBG	electromagnetic band gap
ECM	equivalent circuit model
E-field	electric field
EM	electromagnetic
EMP	electromagnetic pulse
EP	electronic protection
ESD	electrostatic discharge
FBW	fractional bandwidth
FAR	frequency agile radar
FoM	figure of merit
FSS	frequency selective surface
HEMP	high-altitude electromagnetic pulse
HPM	high-power microwave
IST	Imaging Systems Technology

MFEF	maximum field enhancement factor
PA	power amplifier
PCB	printed circuit board
RCS	radar cross section
RF	radio frequency
S-band	IEEE microwave band, 2–4 GHz
S-parameter	Scattering parameter
SAR	synthetic aperture radar
SATCOM	satellite communication
SMT	surface mount technology
SNR	signal-to-noise ratio
SMT	surface mount technology
TE	transverse electric
TEM	transverse electromagnetic
TM	transverse magnetic
TWT	traveling-wave tube
UAV	unmanned aerial vehicle
VNA	vector network analyzer
X-band	X-band IEEE microwave band, 8–12 GHz

Background

The need for camouflage systems at RF/microwave frequencies has been the focus of research since the Second World War [1, 2]. These systems, used particularly for stealth applications, have the capability to alter the radar cross section (RCS) of a target [3, 4]. Among many, conductor-backed absorbers are used extensively in military and aerospace applications to reduce or deflect the backscattered EM signal from their defense equipment (manned or unmanned aircrafts, ground vehicles, naval vessels, guided missiles, etc.) that can be detected by hostile radar [4]. Such absorbers comprised of various materials, shapes, sizes, and design patterns are intended to dissipate the incident wave at the spectrum of interest while reflecting the out-of-band frequency waves. Absorbers can be broadly categorized into material-based and structural-based. The most well-known material-based absorber is the pyramidal absorber, which presents a gradual transition in impedance from air to absorber. However, it can only be used in limited applications, such as in anechoic chambers because the material used is fragile and bulky. On the other hand, structural-based absorbers use resonant behavior to absorb the electromagnetic (EM) wave. The Salisbury screen [5], which uses a lossy homogeneous sheet backed by a completely reflective plane at quarter-wavelength distance at the operating center frequency, is one of the most basic resonant type absorbers. This single layer design has limited bandwidth due to its resonant behavior. To improve the absorption bandwidth, the Jaumann absorber [6] uses multiple resistive layers cascaded quarter-wavelengths apart. However, this technique is impractical in most applications due to its large design thickness. Also, the sheet resistance values of the layers increase exponentially from the ground outward to the free space, which leads to manufacturing limitations. Another type of multilayers absorber based on the quarter wavelength resonator concept is named after Dallenbach [7]. Dallenbach absorber depends on the permittivity and permeability of lossy substrates cascaded quarter-wavelengths apart. With the evolution of frequency selective

surface (FSS) designs, new radar absorbers including circuit analog absorber (CAA) [8, 9] and metamaterial absorbers [10–13] have been introduced. Circuit analog absorbers use cascaded lossy bandstop FSS sheets about quarter-wavelength between layers, similar to the Jaumann absorber, but with better performance in terms of absorption bandwidth. In contrast to all aforementioned absorbers that are limited to quarter-wavelength spacers between adjacent layers, metamaterial absorbers based on high impedance surfaces offer designs with flexible thickness from near contact to quarter-wavelength. These periodic structures provide artificial boundaries to the electromagnetic waves and can be used to implement either very thin narrowband absorbers or thick wideband absorbers. Nevertheless, the performance of passive absorbers with fixed reflectivity-bandwidth characteristics cannot withstand modern frequency agile radar (FAR) systems.

1. Introduction

1.1 Problem

For target detection and tracking, the frequency agile radar (FAR) system performs multi-functional measurement by sending signals through different carrier frequencies [14, 15]. In order to account for the operating frequency shift, wideband tunable/adaptive radar absorbing materials are crucial in avoiding battlefield surveillance. Nowadays, many existing tunable radar absorbers achieve variable impedance at their input by integrating tuning elements such as PIN diodes, semiconductor and ferroelectric varactors, MEMS switches, liquid-crystal polymers, graphene, and liquid metal [16–25]. However, intrinsic characteristics of these tunable components have repercussions on one or more device performance factors, such as: tuning range or speed, reliability, linearity, polarization sensitivity, cost, weight, and fabrication complexity. In terms of reliability, the aforementioned tunable absorbers are vulnerable when operated in extreme environmental conditions including high temperatures and EM radiation from high power microwave and electromagnetic pulse (HPM/EMP) tracking radar systems. This is because such tuning components have limited power handling capability. Moreover, the choice of lossy material is important when the thermal stress due to time-average ohmic losses is of primary concern. In a case where the temperature exceeds the combustion level of the lossy material, burning will occur and the failure in the system will increase the probability of detection.

1.2 Objective

The ultimate goal of this project is to investigate the feasibility of devising scalable tunable/adaptive absorbers that can maintain stable operation in harsh and dynamic electromagnetic battlefield surveillance subject to high power microwave energy. The develop-

ment of compact, lightweight, and high-performance electromagnetic absorbers for stealth applications is vital in strengthening the Department of Defense capabilities against high power radar tracking systems. In this project, we propose a low-profile tunable absorber based on discrete plasma-shells that provide a wide dynamic range of absorption spectral band. The use of discrete plasma-shells allows the deployment of large-scale absorbers in which the properties of the confined gas can be easily manipulated. For demonstration purposes, the proposed tunable absorbers are designed to meet the following requirements:

- Excellent in-band absorption greater than 90 % (i.e. at least 10 dB absorptivity)
- Real-time tunability of absorption spectral band that can dependably perform under harsh EM environments
- Stable absorption response over wide incident angle ($> \pm 45°$)
- Low-profile design ($\ll \lambda/4$ separation between adjacent FSS layers)
- Polarization independent (this feature is best suited for randomly moving and/or rotating systems as it minimizes polarization mismatch loss)
- Capable of withstanding ionizing radiation, shock, vibration and temperature range up to 250 °C
- Ability to integrate into existing structures to meet the needs of a broad range of Air Force applications.

1.3 Organization of the Report

This report is organized into five Sections (2–6) summarized as follows:

1. In Section 2 we summarize our previous work devoted for the realization of switchable Frequency Selective Surfaces (FSSs) based on the plasma-shell concept.

2. In Section 3, we investigate the feasibility of devising a low-profile, practical, large-scale, electronically tunable/adaptive absorber based on plasma technology. We demonstrate the concept by integrating plasma-shells with a well-designed metallic backed absorber. The control of the spectral/level of the absorption band is allowed by systematically changing the plasma density. The proposed FSS-based absorbers are loaded with different types of resistive sheets (lossy inductive FSS, lossy capacitive FSS, and lossy resonant FSS layer).

3. In Section 4, we investigate potential implementations of the proposed absorber subjected to high power microwave and electromagnetic pulse (HPM/EMP) by selecting core materials that are suitable for higher-temperature service. A magneto-dielectric substrate has been incorporated in the design as a substitute for the resistive sheet to account for the loss. This alternate design allows the EM energy to be dissipated in lossy magneto-dielectric substrates. Instead of relying on exotic lossy materials (such as magneto-dielectric composite materials obtained from advanced synthesis technique) [26–28] to achieve good performance in a specific frequency range, our design simply makes use of commercially available lossy magneto-dielectric substrates (from Laird's Eccosorb MF500F series) suitable for HPM/EMP compared to the resistive sheet used in the prior design.

    - First, a single pole FSS-based absorber using the magneto-dielectric substrate is investigated.
    - Then, we expand the single pole FSS-based absorber to a higher order spatial FSS based absorber to increase the absorption bandwidth. The proposed

multilayer absorber is based on a technique developed for the design of a thickness customizable high-order bandpass FSS [29–31]. Such technique allows simple integration of the tuning elements, while simultaneously providing the design option to realize the absorber with specific/desired thicknesses. These multi-layered absorbers with potential integration of tuning components enable tunable/adaptable operation modes by controlling the plasma density at each FSS layer.

4. In Section 5, the performance of a two-pole high power microwave (HPM) absorber is investigated under high power excitation. The maximum power handling capability of the device has been numerically predicted and validated experimentally.

5. Finally, a comprehensive conclusion is given in Section 6.

2. Switchable FSS Based on Discrete Plasma-Shells Concept

Plasma's electrical properties and its advantages in stealth applications have been extensively studied [32, 33]. Theoretically, plasma medium can be manipulated at the appropriate frequency to transmit/delay, reflect, or absorb electromagnetic radiation. Notably, it has the unique property to withstand high power microwave energy [34, 35]. However, attempts to realize a practical large-scale plasma device have presented challenges in integrating the plasma with the EM device [36, 37] and assuring control over its properties (plasma density, gas composition, and pressure). Plasma devices previously employed have often been bulky, fragile, and non-hermetic. Mostly, there is no control over the gas content and pressure. Consequently, they have a short operating life and would not have been able to stand up to the rigors of aerospace, military, or satellite applications.

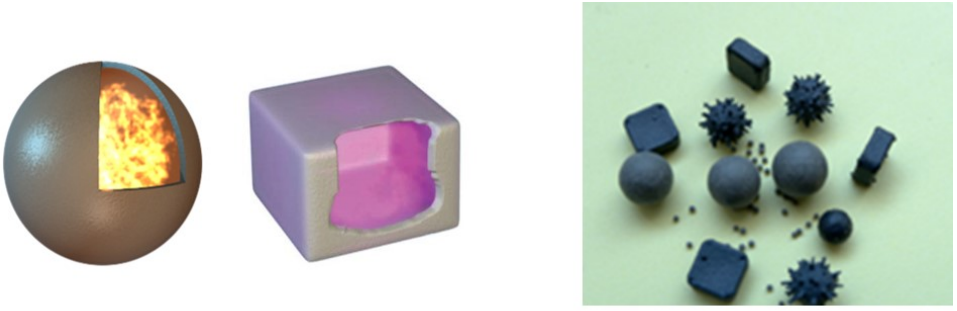

(a) (b)

Figure 2.1: (a) Plasma-shells cutaway showing internal plasma. (b) IST manufacturing capability produces shells of various size, shape, and texture.

Recently, controlled gas-encapsulating ceramic chambers [38] have been patented and made commercially available by Imaging Systems Technology (IST) Inc. to circumvent the aforementioned problems. These plasma-shells generate plasma when properly biased. The ceramic, gas-encapsulating shells are ideal for high-power microwave and electromag-

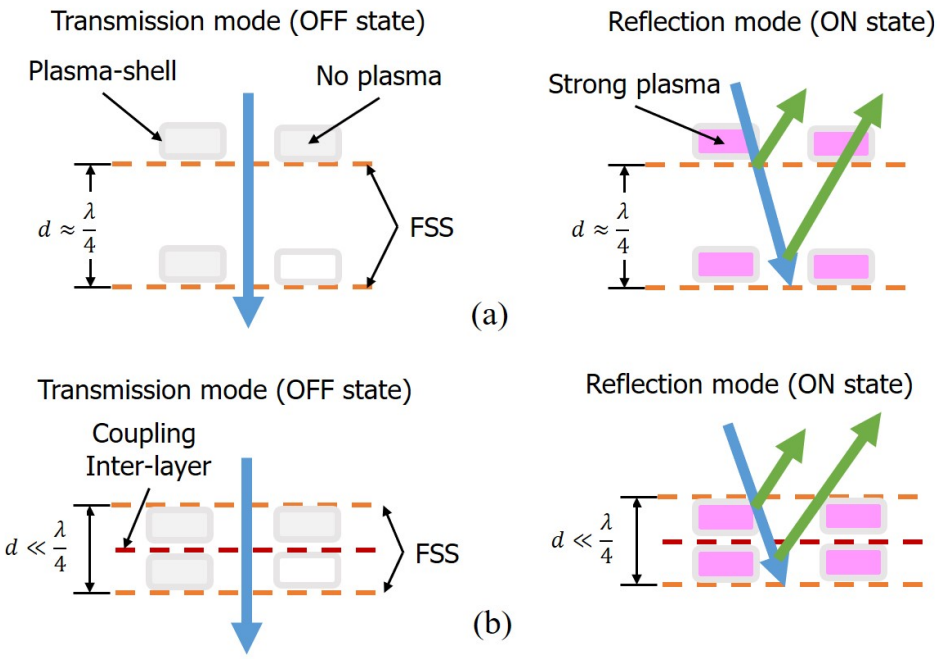

Figure 2.2: (a) FSS layers separated by quarter-wavelength. (b) Compact design using coupling inter-layers.

netic pulse protection because they are rugged, hermetic, operate at extreme temperatures, and are insensitive to ionizing radiation. When energy is applied across the exterior surface of the plasma-shell, the encapsulated gas ionizes as shown in Figure 2.1(a). Ionized gas can emit, reflect, or absorb EM energy. Typical sizes of plasma-shells range from 0.5 to 10 mm, and are compatible with surface-mount technology assembly techniques. Shells are extremely lightweight and can be manufactured in different shapes: spheres, cylinders, cubes, oblate spheroids, rectangular prisms, and other complex shapes as shown in Figure 2.1(b). Primary materials of shells include: Y_2O_3, Z_rO_2, S_iO_2, Al_2O_3, carbon steel, and various glasses. Noble gases (helium, neon, argon, krypton, xenon) are often used as a mixture inside the hermitic shell. The ability to customize the shells (material, size, shape, texture, density) allows them to be easily integrated into many enabling applications. In our previous project supported by the Air Force Research Laboratory (under Contract No.

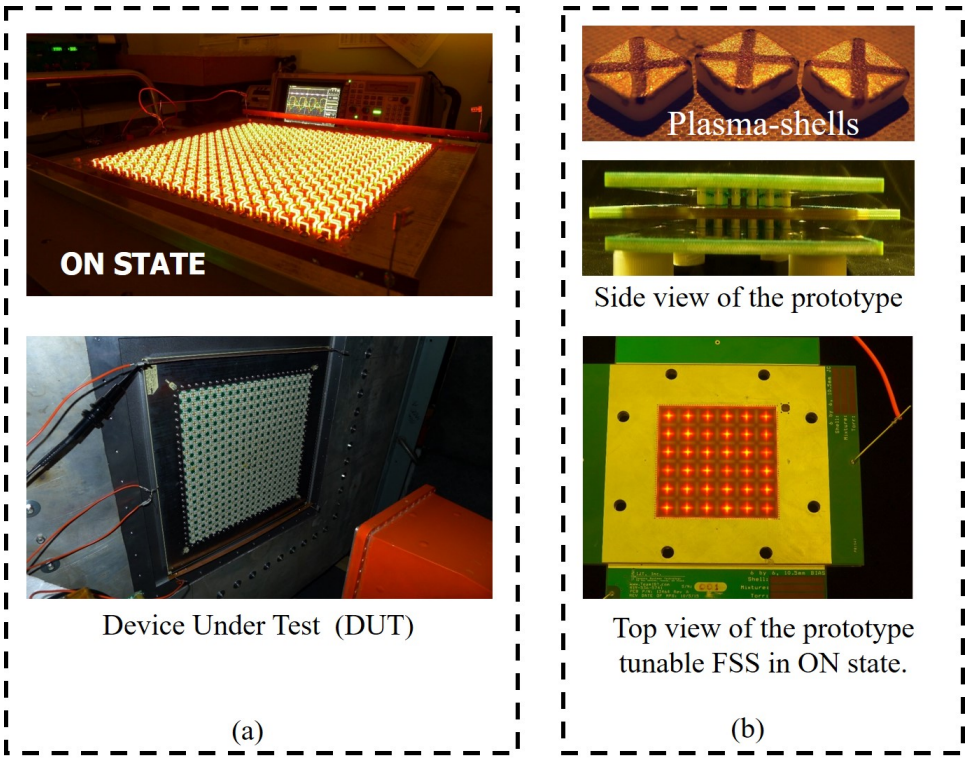

Figure 2.3: Fabricated samples in our previous work. (a) Prototype with quarter-wavelength concept. (b) Prototype with coupling layer concept.

FA9453-13-M-0172), we have used these plasma-shells as real-time fast electronic switches (as short as 100 ns) in the design of practical large-scale switchable electromagnetic field blocking FSSs [39, 40] for the protection of EM systems subjected to HPM/EMP. In these projects, we demonstrated a switchable second order FSS based on discrete plasma-shells. Two topologies (as shown in Figure 2.2) were adopted to provide a fast switchable pass-band response with both in-band and out-of-band protection level of at least 40 dB dB average (see [39, 40]). A 12 in^2 large panel (array of 19 $\times$ 19 elements) of the first topology and a small panel (array of 6 $\times$ 6 unit elements) of the second topology were fabricated (see Figure 2.3) and measured for validation.

3. Plasma-Based Tunable Absorber Loaded with Resistive Sheet

3.1 Design specification and model analysis

Unlike our previous designs where these plasma-shells electrical properties were manipulated and used to design spatial filter switches, in this project, they serve as tuning components of reconfigurable absorbers. The topology of the proposed design is based on a resistive metamaterial sheet absorber. A lossy inductive, capacitive or resonator layer, which is embedded with discrete plasma-shells, and a practical biasing layer (as shown in Figure 3.1) is investigated.

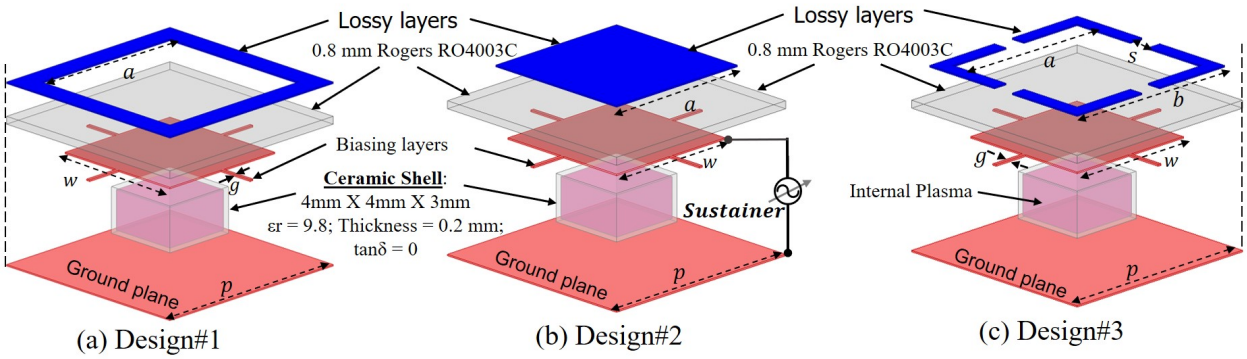

Figure 3.1: Unit cell representation of the dynamic plasma-based absorber along with the detailed geometry (units are in mm). (a) Design #1 indicates the absorber with the inductive lossy layer. (b) Design #2 is the one with the capacitive lossy layer. (c) Design #3 is the one with lossy resonator layer.

The lossy layer is made of resistive film with specific surface resistivity R_S [$\Omega/\square$]. The pattern of the metallic biasing layer combines a square patch array with a wire grid. In the proposed designs, the lossy layer and biasing network are printed on RO4003C, a hydrocarbon ceramic laminate from Rogers Corporation's RO4000 series materials, which are known for their reliability when subject to severe thermal shocks. The thickness of the

substrate is h_1 = 0.813 mm and relative permittivity is ε_{r1} = 3.38 with ±0.05 tolerance. The plasma shells (shell size: 4 mm × 4 mm × 3 mm), placed between the ground plane and the biasing layer, are used not only as the tuning component, but also for structural support. The shells are made of hollow ceramic dielectric (Al_2O_3) material with wall thickness of 0.2 mm and dielectric constant of 9.6. The shells are bonded to the metallic layers with 0.5 mm thickness of silver epoxy (not shown in the figure) used as electrodes to facilitate the coupling of energy through the dielectric wall of the shell. The internal gas volume can be modeled as a complex frequency dependent material, with the permittivity ε_p expressed as follows [41]:

$$\varepsilon_p = \varepsilon_0(\varepsilon_r' - j\frac{\sigma_p}{\omega\varepsilon_0}), \tag{3.1}$$

where $\varepsilon_0 = 8.854 \times 10^{-12}$ F/m is the permittivity of free-space, ε_r' is the real part of relative permittivity, σ_p [S/m] is the conductivity and ω [rad/s] is the operating angular frequency.

$$\varepsilon_r' = 1 - \frac{\omega_p^2}{\omega^2 + \nu^2} \text{ and } \sigma_p = \frac{\omega_p^2 \cdot \nu \cdot \varepsilon_0}{\omega^2 + \nu^2}, \tag{3.2}$$

where ω_p [rad/s], and ν [rad/s] are plasma frequency and electron collision frequency, respectively. It is noted that the plasma frequency ω_p depends on the electron density n_e [m^{-3}] as:

$$\omega_p = \sqrt{\frac{n_e \cdot e^2}{\varepsilon_0 \cdot m_e}} \approx 56.4\sqrt{n_e}, \tag{3.3}$$

where e is the electron charge ($e = 1.6 \times 10^{-19}$ C), and m_e is the electron mass ($m_e = 9.1 \times 10^{-31}$ kg). The electron density of the ionized plasma is electrically controlled by

applied voltage. The electron collision frequency for a noble gas is obtained from [42]:

$$\nu[s^{-1}] = \frac{8}{3 \times \pi^2} N \left(\frac{m_e}{2K_B T_e} \right)^{5/2} \int_0^\infty \vartheta^5 Q^{(m)}(\vartheta) exp \left(-\frac{m_e \vartheta^2}{2K_B T_e} \right) d\vartheta, \tag{3.4}$$

where T_e [K], N [cm^{-3}], K_B [J/K], ϑ [m/s], and $Q^{(m)}(\vartheta)$ are temperature, gas number density, Boltzmann's constant, velocity, and momentum transfer cross section of the electrons, respectively. The gas number density N [m^{-3}] is obtained from the ideal-gas equation of state as:

$$N = \frac{P}{K_B T_e}. \tag{3.5}$$

where P [Pa] is the gas pressure. It can be seen that while the electron collision frequency can be controlled by the gas contents, the plasma frequency is controlled by the biasing voltage. Thus, for fixed gas contents, the dielectric constant of the plasma medium can be altered by adjusting the biasing voltage. In the proposed active absorbers, the metallic resonators are used as a practical biasing network. As a result, the effective relative dielectric constant loading the FSS capacitors can be controlled to add tunability to the system.

To elucidate the working principle of the absorption and its frequency tuning capability, a transmission line model approach is adopted. The equivalent circuit model (ECM) of the design is shown in Figure 3.2. The biasing layer is modeled by a parallel L_b, C_b resonant tank and the bulk plasma as a shunt component with admittance Y_P. The biasing network and the ground plane are separated by a transmission line with length h_0 = 3 mm (height of the shell) and characteristic admittance Y_0 (characteristic admittance of free space). The lossy layer is also modeled as a shunt admittance Y_L, which is separated from the biasing network by a short transmission line of length h_1 and characteristic admittance

$Y_1 = Y_0\sqrt{\varepsilon_{r1}}$. For the first topology, the lossy layer is inductive and is seen as a series R_I, L_I, and for the second topology it is capacitive, thus seen as a series R_C, C_C. on the other hand, for the third design, the lossy layer is a resonant component seen as a series R_r, L_r, C_r. From the ECM, the input admittance of the circuit can be obtained as follows:

$$Y_{in} = Y_L + Y_1\frac{(Y_{bias} + Y_p + Y_d) + jY_1\tan(\beta_1 h_1)}{Y_1 + j(Y_{bias} + Y_p + Y_d)\tan(\beta_1 h_1)}, \tag{3.6}$$

$$Y_d = -jY_0\cot(\beta_0 h_0);\ Y_{bias} = j(\omega C_b - \frac{1}{\omega L_b}), \tag{3.7}$$

$$Y_L = \begin{cases} (R_I + j\omega L_I)^{-1} & \text{for the lossy inductive sheet} \\ (R_C - \frac{j}{\omega C_C})^{-1} & \text{for the lossy capacitive sheet} \\ (R_r + j\omega L_r - \frac{j}{\omega C_r})^{-1} & \text{for the lossy resonator sheet} \end{cases} \tag{3.8}$$

The bulk plasma is modeled based on parallel plane geometry and because equal electrode area is used at each side of the shell, symmetric discharge is adopted. Generally, a plasma medium can be treated as a conductor with conductivity σ_p or as a dielectric with permittivity ε_p based on its electron collision frequency, its plasma frequency and

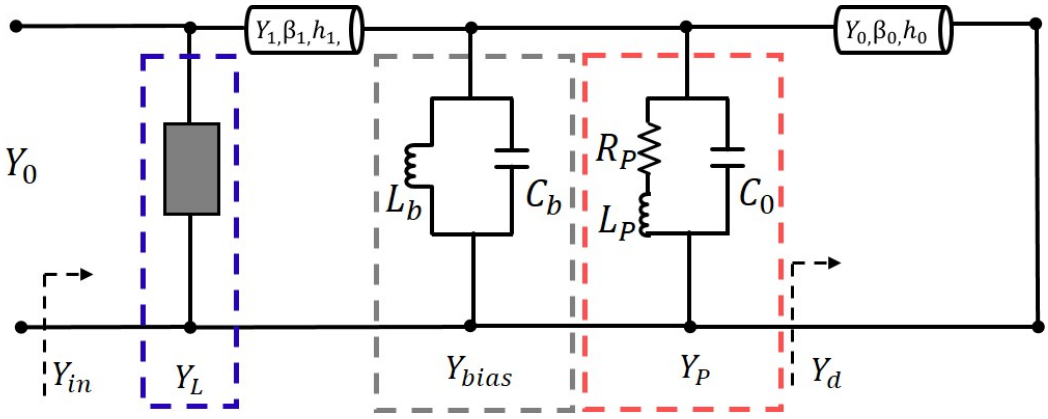

Figure 3.2: Equivalent circuit model of the tunable absorbers for normal angle of incidence.

the operating frequency of the system [41]. The first scenario is met for low frequencies where $\omega \ll \omega_p, \nu$. The conductivity of the plasma is then reduced to its dc form such that $\sigma_p \rightarrow \sigma_{dc} = \frac{\omega_p^2 \cdot \varepsilon_0}{\nu}$. Such characteristics of the plasma have been used in [39, 40, 43] to design switchable frequency selective surfaces for electronic protection. In this project, the second scenario is considered where the bulk plasma is used as a dielectric with variable permittivity. In this regime, we have $\nu < \omega < \omega_p$, which is practical for plasma driven at RF discharge. The admittance Y_p of the bulk plasma is given in [41] as:

$$Y_p = \frac{j\omega\varepsilon_p A}{h_0}, \tag{3.9}$$

where A is the effective cross-sectional area of the plasma. By assuming uniform electron density, this expression is approximated to:

$$Y_p = j\omega C_0 + (j\omega L_p + R_p)^{-1}. \tag{3.10}$$

where $C_0 = \varepsilon_0 A/h_0$ is the capacitance of the vacuum chamber, $L_p = \omega_p^{-2} C_0^{-1}$ is the inductance of the plasma, and $R_P = \nu L_p$ is the plasma resistance. As shown in Figure 3.2, the shunt component with impedance Y_p is modeled as a series (L_p, R_P) in parallel with C_0. Theoretically, the resonant frequency ω_0 of the absorber is obtained when $\mathrm{Im}[Y_{in}(\omega_0)] = 0$, with a matching condition such that $\mathrm{Re}[Y_{in}(\omega_0)] = Y_0$. Thus, the operating frequency of the absorber can be simply tuned by adjusting its input impedance. This task can be achieved with the variation of the bulk plasma admittance Y_p. At OFF state $(\omega_p = 0)$, the series $(L_p R_P)$ circuit is opened and the bulk plasma model is reduced to the shunt capacitance C_0. At ON state $(\omega_p = 0)$, the admittance Y_p of the plasma discharge is a parallel combination of the shunt capacitance C_0 with the series $(L_p R_P)$ circuit. As the plasma frequency ω_p increases, the values of the inductance and resistance decrease.

Therefore the effective inductance of the system decreases leading to the tuning of the resonant absorption frequency as it shifts to higher frequency. In fact, from Equation (3.10), it can be perceived that for a fixed electron collision frequency (gas content and pressure), the impedance of the plasma can be controlled by either its plasma frequency or its cross-sectional area, as will be conveyed in the next section.

3.2 Implementation and simulation results

For demonstration purpose, the tunable absorbers are designed to operate in the X-band (8 GHz to 12 GHz), as this specific band is commonly used for radar and military electronic warfare applications, as well as satellite, terrestrial and space-based communication. However, the design concept can be suited to arbitrary operating frequencies. A full wave EM analysis using ANSYS HFSS is utilized to characterize the response of the structures at OFF state as shown in Figure 3.3. Based on the physical parameters and the full wave frequency response of the absorber without the plasma-shells, the electrical parameters of the ECM are extracted in conjunction with a circuit simulator (Keysight's Advanced Design System).

Table 3.1: Physical/electrical parameters of the proposed absorber.

Physical parameters	p (mm)	a (mm)	b (mm)	ω (mm)	g (mm)	s (mm)	R_S ($\Omega/\square$)
Design #1	13	11	–	9.55	0.25	–	110
Design #2	13	11	–	7.9	0.25	–	100
Design #3	15	10.9	12.6	9.35	0.25	1	9.3
Electrical parameters	L_b (nH)	C_b (pF)	L_I (nH)	C_c (pF)	L_r (nH)	C_r (pF)	R (Ω)
Design #1	2.3	0.2	1.6	–	–	–	320
Design #2	2.6	0.08	–	0.1	–	–	146
Design #3	8	0.09	–	–	16.5	0.019	365

First, the values of the parallel L_b, C_b resonant tank are obtained using simple analytical expressions for wire grid and patch array [44]. Next, only the lossy layers with the RO4003C

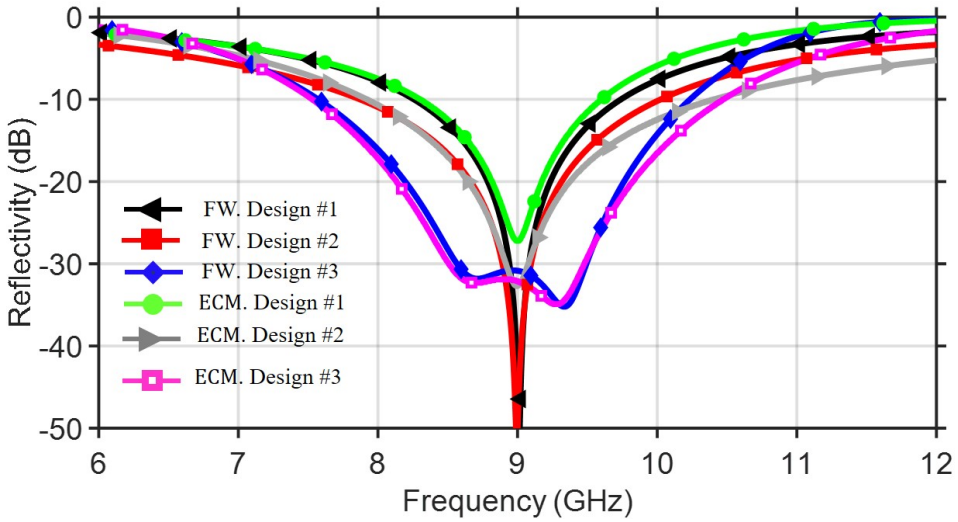

Figure 3.3: Simulated FW simulation results for the reflectivity of the passive absorbers along with the ECM results.

are simulated using full wave EM simulation and then the responses are matched to those obtained from their counterpart ECM comprised of a series R_I, L_I or R_C, C_C or R_r, L_r, C_r followed by the short transmission line of length h_1 using a curve fitting technique. The value of the capacitance that accounts for the dielectric constant shells C_0 is numerically obtained from the full wave simulation of the design (in Figure 3.1) with and without the plasma shells. Finally, by linking and slightly adjusting all the electrical parameters obtained, the frequency responses of the complete ECM in Figure 3.2 are simulated for the OFF state case.

The physical and electrical parameters of the absorbers are provided in Table 3.1. Both the full wave EM results and the ECM results are illustrated in Figure 3.3 and the comparison reveals the accuracy of the transmission line modeling. The total thickness of each absorber is about 3.813 mm, corresponding to $0.11\lambda_0$, where λ_0 is the free space wavelength of the absorption center frequency (f_0 = 9 GHz). The results of the passive absorber predict about 18 %, 24 % and 30 % fractional bandwidth at 10 dB return loss level for the lossy inductive, capacitive and resonant FSS layers design type, respectively. The

bandwidth over thickness performance of the proposed absorbers is computed and also compared with a Salisbury screen (operating at the same center frequency) by examining their respective figure of merit (FoM), as depicted in Table 3.2. The FoM is found by using the Rozanov [45] physical bound imposed on the thickness to bandwidth ratio for any nonmagnetic metal backed absorber as:

$$FoM = \frac{|\ln(\rho_0)|(\lambda_{max} - \lambda_{min})}{2\pi^2 d}, \tag{3.11}$$

where ρ_0 is the reflectivity, d is the total thickness of the absorber, and λ_{min} and λ_{max} are the respective minimum and maximum wavelength in the spectrum range allowed by the specific reflection coefficient. As given in Equation (3.11), a higher FoM indicates the design with superior performance. Table 3.2 shows that beyond the 20 dB absorption level (which is typically preferred in most applications), wider absorption bandwidth is obtained for Design #3. Although Design #1 and Design #2 have similar performance compared to the Salisbury screen, their active counterparts will have superior overall characteristics.

Table 3.2: Comparison in FoM between the proposed absorbers and Salisbury screen.

Reflectivity	ρ_0 = 0.1 (10 dB)	ρ_0 = 0.01 (20 dB)	ρ_0 = 0.001 (30 dB)
Salisbury	0.4064	0.2390	0.1123
Design #1	0.1851	0.1013	0.0473
Design #2	0.2483	0.1470	0.0677
Design #3	0.3130	0.3605	0.3115

At ON state, the admittance of the bulk plasma can be engineered to provide the tunability capability to the design. The electron collision frequency of the plasma is set to its optimal value $\nu = 3.6 \times 10^{10}$ rad/s. Then, the response of the absorbers is examined by changing the plasma frequency within the range of 0 (OFF state) to 8×10^{11} rad/s. Both

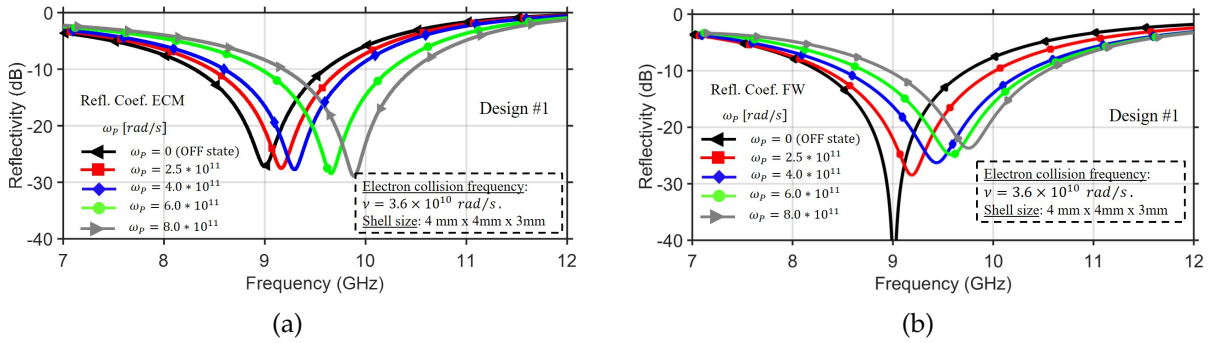

(a) (b)

Figure 3.4: Simulated results of the plasma-based absorber (Design #1) subject to different plasma frequencies. (a) Simulated ECM tuning response. (b) Simulated full wave tuning response.

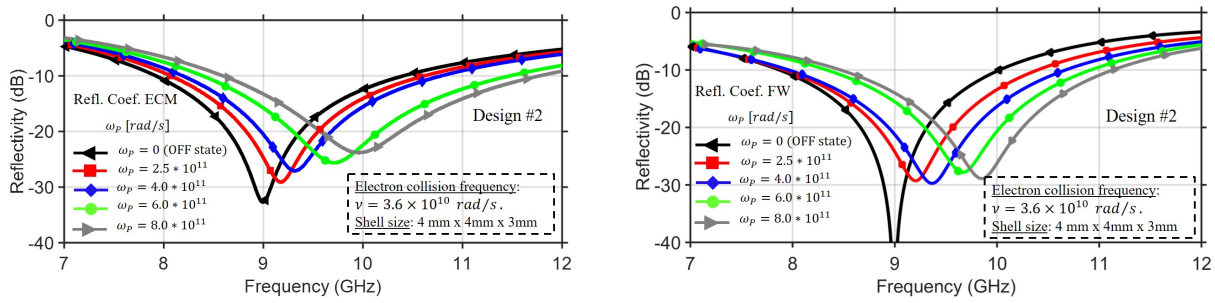

(a) (b)

Figure 3.5: Simulated results of the plasma-based absorber (Design #2) subject to different plasma frequencies. (a) Simulated ECM tuning response. (b) Simulated full wave tuning response.

the simulated ECM and the full wave EM results for all three designs are illustrated in Figure 3.4, Figure 3.5 and Figure 3.6, respectively . By comparing the frequency response of the absorber using full wave EM simulation to those obtained from the ECM, it is observed that the ECM accurately predicts the behavior of the absorber at ON state. The results show that the absorption center frequency increases from 9 GHz to 10 GHz, providing a dynamic tuning of the absorption spectral band for Design #1 and Design #2. Instead, for Design #3, the increase of the plasma frequency mostly affects the higher resonance frequency, thus providing a tuning of the absorption spectral bandwidth but at the expense of the absorption rate.

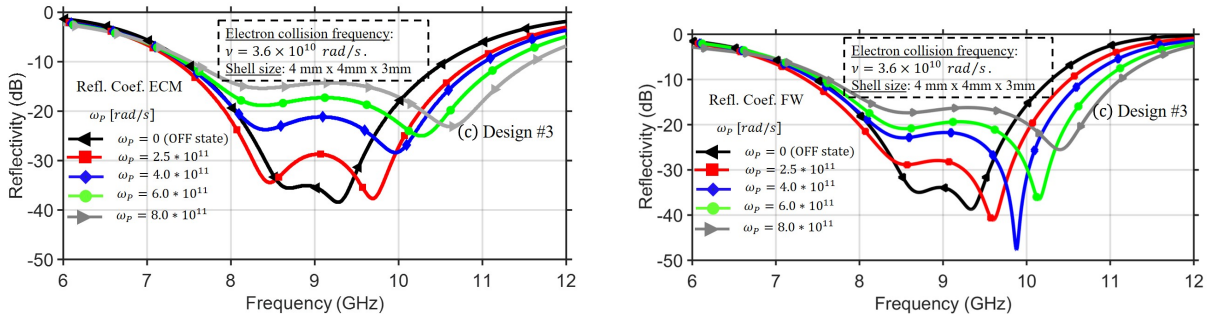

Figure 3.6: Simulated results of the plasma-based absorber (Design #3) subject to different plasma frequencies. (a) Simulated ECM tuning response. (b) Simulated full wave tuning response.

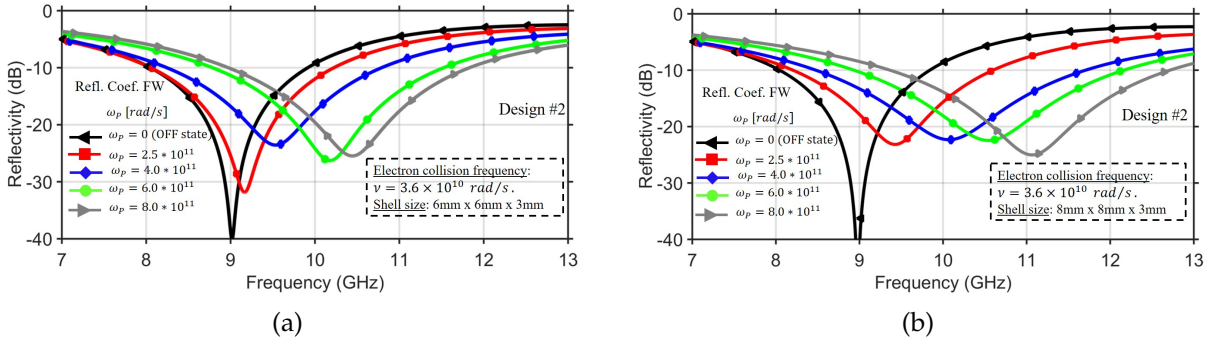

Figure 3.7: Simulated full wave response of the plasma-based absorber subject to different plasma frequencies and larger shell size. Tuning capability observed for Design #2.

The tuning range of the absorber can be further improved by increasing the cross-sectional area of the shell. The size of plasma-shell that can be manufactured ranges from 0.5 mm to 10 mm. The response of the absorber is further explored using larger plasma-shell size with dimensions 8 mm $\times$ 8 mm $\times$ 3 mm such that the thickness of the design remains unchanged (i.e. only the cross-sectional area of the unit cell shell is increased). By changing the plasma frequency, the center frequency of the absorber (Design #2) can be increased with the size of the plasma shells from 9 GHz to 11 GHz (see Figure 3.7), which is about double the tuning range previously obtained. Also the absorption bandwidth for Design #3 has increased considerably under the same tuning procedure.

3.3 Fabrication and measurement results

To validate the numerical results, one of the prototype circuits (Design #2) is fabricated on 0.813 mm thick RO4003C substrate. An array of lossy capacitive patches made of R_{CS}=100 $\Omega/\square$ OhmegaPly resistive film (manufactured by Ohmega Technologies, Inc.) and the metallic biasing layer are laminated and patterned on either side of the substrate using wet etching process. The board is made by Brigitflex Inc., a circuit board manufacturer known for their expertise in the fabrication of customized PCBs embedded with planar resistors. A square panel of about 5 in $\times$ 5 in (equivalent to $4\lambda_0 \times 4\lambda_0$) including an array of 10 $\times$ 10 elements is used as the test sample. The front and back of the circuit are shown in Figure 3.8. The plasma-shells (shell size: 4 mm $\times$ 4 mm $\times$ 3 mm) filled with 0.1 % Argon - 99.9 % Neon mixture at 175 Torr gas pressure are commercially available from Imaging Systems Technology Inc. The value of the gas pressure (P = 175 Torr) is estimated by solving a simple theoretical expression for neon gas derived in [46] at 300 K electron temperature:

$$\nu[s^{-1}] = 8.63 \times 10^{-18} \times \left(\frac{P}{K_B T_e}\right) \times T_e^{0.833} \text{ for } 10^2\,\text{K} \leq T_e \leq 5 \times 10^3\,\text{K}, \tag{3.12}$$

The plasma-shells are electrically bonded to the metallic layers with 0.5 mm thickness of silver conductive epoxy. A frame with an array of cavities fabricated using a 3D printer (uPrint SE Plus) is used for fine alignment. The silver conductive epoxy is deposited on both the biasing and ground plane using a syringe. Then the shells are manually placed in the cavities. The fabrication process is illustrated in Figure 3.9. The assembled board including the plasma shells and ground plane is shown in Figure 3.8(c).

The fabricated device is excited with a sinusoidal wave produced by Keysight's N5181A MXG RF analog signal generator operating in the range of 100 kHz to 6 GHz with the

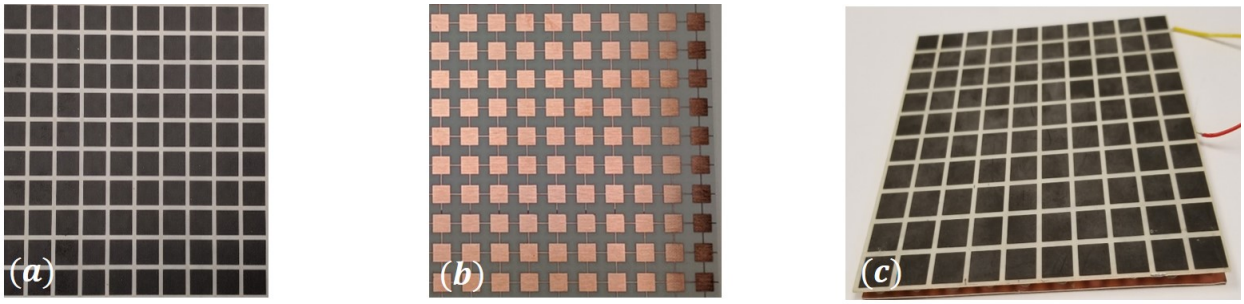

Figure 3.8: Fabricated sample. (a) Front side: lossy sheet. (b) Back side: biasing network. (c) Assembled tunable absorber: side view.

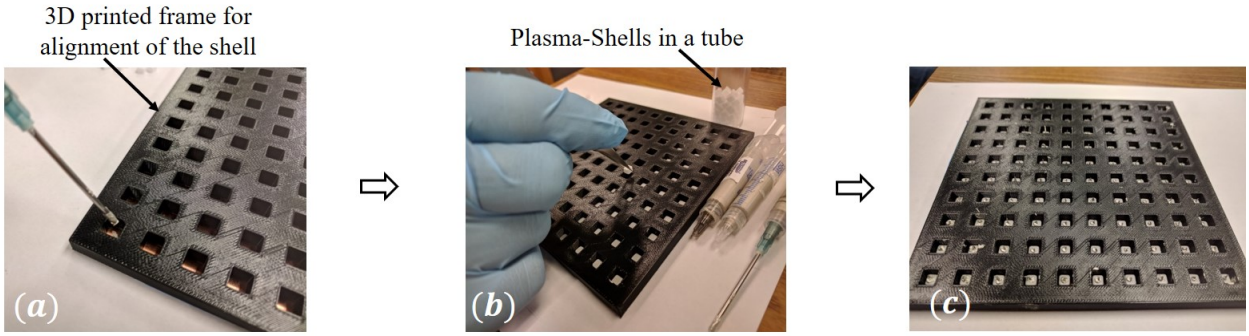

Figure 3.9: Fabrication process. (a) Conductive silver epoxy deposited on ground plane using a syringe. (b) Shells manually placed in holes of 3D printed frame. (c) Conductive silver epoxy also deposited on top side of shells before assembly.

output voltage $V_P \leq 1.7\,\mathrm{V}$. The output voltage from the signal generator is amplified with a 50 dB (nominal) CW ENI/E&I 325LA power amplifier (PA), with driving frequency ranging from 250 kHz to 150 MHz and maximum input voltage limited to 1 V. The output voltage of the PA is then connected to the bias traces of the absorber. If desired, for any specific numerically plasma frequency used for each tuning state, the total power required to sustain the plasma-shells can be estimated using the approximated power per unit volume for noble gas plasma dominated by two-body recombination [32]:

$$\frac{P}{V} = k n_e^2 E_i \approx k \left(\frac{\omega_p}{5.64 \times 10^4} \right)^4 E_i, \tag{3.13}$$

where k [cm^3/s] is the two-body dissociative rate constant, E_i [$joules$] is the energy required to ionize a noble gas, and V [cm^3] is the plasma volume. The value of $k = 1.8 \times 10^{-7}\,\mathrm{cm}^3/\mathrm{s}$ and $E_i = 36.2\,\mathrm{eV} = 5.8 \times 10^{-18}\,\mathrm{J}$ can be found in [32]. Because 100 plasma-shells (shell size: $4\,\mathrm{mm} \times 4\,\mathrm{mm} \times 3\,\mathrm{mm}$) are used for the fabricated prototype, the total plasma volume is about $V = 4.8\,\mathrm{cm}^3$. Therefore, under perfect conditions, for any specific plasma frequency ω_p, the CW power P [W] required to sustain the plasma volume can be estimated using Equation 3.13. Then the voltage V_P can be theoretically obtained by taking into account the 50 dB gain of the power amplifier. However, due to the complexity of the nature of charged particles in the plasma medium, the power loss due to the mismatch of the biasing network, the choice of the driven RF frequency, and other factors including fabrication errors, the theoretical value of P has not been correlated with the experimental value. Instead, the absorber tuning states given the driven RF frequency and the experimental voltage V_P from the signal generator are empirically approximated.

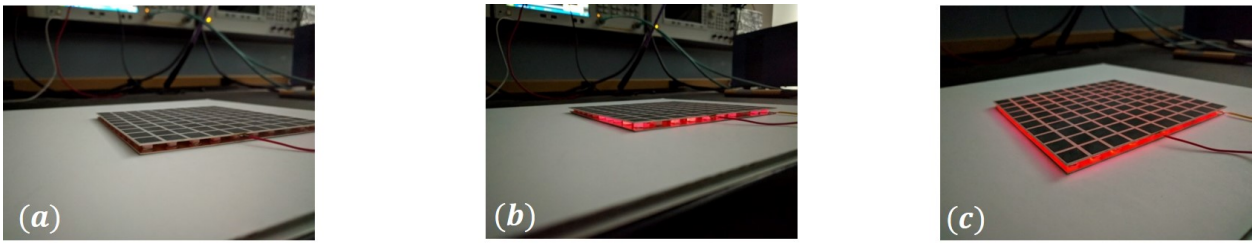

Figure 3.10: Dimming effect of the shells when plasma discharge is driven with 1 MHz RF signal. By increasing the voltage from the signal generator a glow discharge is obtained as a sign of avalanche discharge. (a) $V_P = 0.5\,\mathrm{V}$. (b) $V_P = 0.7\,\mathrm{V}$. (c) $V_P = 0.9\,\mathrm{V}$.

By setting the driven frequency (fs) at 1 MHz and increasing the voltage from the signal generator, the glowing effect of the plasma-shells can be seen in Figure 3.10. An electric glow discharge visible to the eye is produced. When $V_P = 0.7\,\mathrm{V}$, the power output into the load which is monitored by a built-in front panel meter of the PA reads about 50 W (power density of $2.9\,\mathrm{kW}/\mathrm{m}^2$). The sustained continuous wave output power generated by the power supply is capable to ionize the large-scale plasma-device and eliminate the

Figure 3.11: Sketch and photograph of the test setup (free space) for the absorber measurement.

need of laser excitation or high pulsed voltage supply which are relatively costly.

The experimental setup to validate the device performance is illustrated in Figure 3.11. A pair of PE9887-11 broadband horn antennas are placed about 0.5 m from the device under test (DUT) to ensure the DUT is at far-field from the test antennas. An aperture of the size of the absorber is carved out at the center of a large wood frame to mount the test sample. The frame is covered with an adhesive surface wave absorber (MR-31-0003-20 from Mast Technologies) to reduce diffraction effects from the edges of the DUT. The calibration of the system is carried out by measuring the reflection coefficient of the system when the aperture is covered by a conductor plane. Then the reflection coefficient of the system is obtained with the device under test. These results are obtained with a calibrated Agilent HP 8719ES (50 MHz to 13.5 GHz) vector network analyzer (VNA). Gating window is applied to reduce ripples in the measurement caused by multiple reflections of the waves and also to reduce cross coupling between the horn antennas. The frequency response of the absorber is obtained by normalizing the measured results obtained in the presence of the device with the one obtained from the conductor plane of the same size.

The performance of the absorber (at OFF state) across different angles of incidence for both transverse electric (TE) and transverse magnetic (TM) polarizations is numerically and experimentally obtained. Both simulated and measured results (Figure 3.12 and Figure 3.13) show acceptable and stable reflection response when the system is illuminated

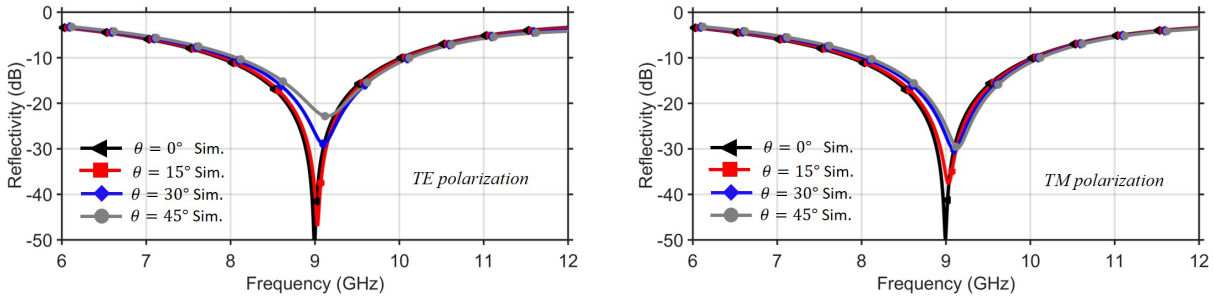

(a) (b)

Figure 3.12: Full wave simulated reflection coefficient of the passive absorber (Design #2) at various oblique angles of incident wave. (a) TE polarization. (b) TM polarization.

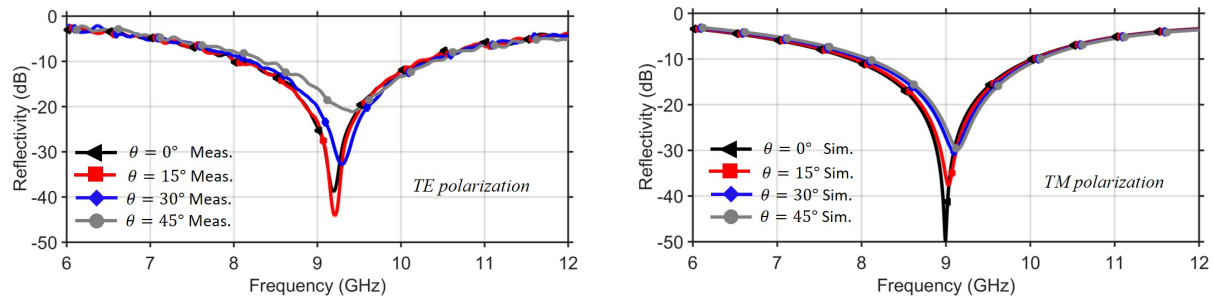

(a) (b)

Figure 3.13: Full wave simulated reflection coefficient of the passive absorber (Design #2) at various oblique angles of incident wave. (a) TE polarization. (b) TM polarization.

from various oblique angles ($0^\circ \leq \theta \leq 45^\circ$). At normal incidence, we can notice a slight deviation of the center frequency from 9 GHz to 9.2 GHz of the measured results compared to the ones obtained from full wave EM simulations. The slight discrepancies can be due to many factors including the finite size of the prototype, the thickness and homogeneity of the silver epoxy used, fabrication tolerance (caused by inaccurate material properties) and imperfect assembly of the absorber.

The reflection coefficients of the device at ON state are obtained when the plasma is sustained using the amplified RF source directly coupled to the gas across the thin ceramic dielectric wall. The driven frequency from the signal generator is set to $f_S = 1$ MHz and a voltage range between $0 \leq V_P \leq 0.9$ V is fed to the PA since its maximum allowed input

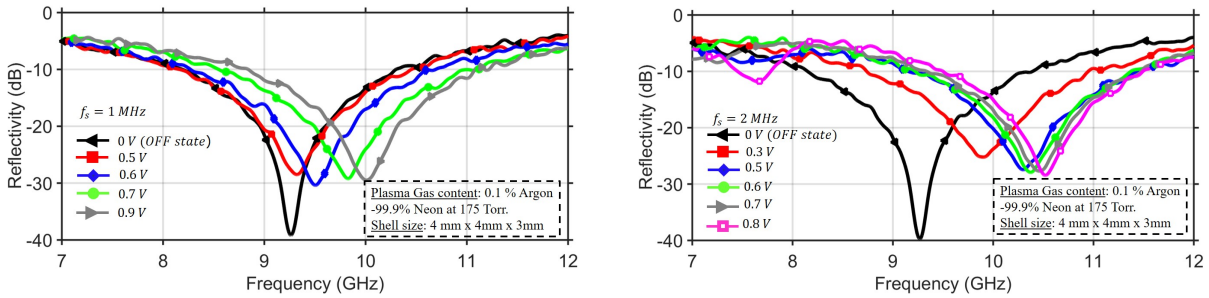

(a) (b)

Figure 3.14: Measured reflection coefficient of the active absorber (Design #2) at normal angle of incidence for various biasing voltages V_P. (a) Driving frequency f_S = 1 MHz. (b) Driving frequency f_S = 2 MHz.

voltage is 1 V. The measured results at normal angle of incidence indicate a tuning of the absorption band in the X-band as shown in Figure 3.14(a). The absorption resonant frequency has increased from 9.2 GHz to 9.9 GHz and wider absorption band is obtained by increasing the biasing voltage. The tuning speed is found to be as short as 10 ns to 100 ns. Experimentally, it has also been previously demonstrated that the percentage of RF power absorbed by the electrons increases with the driven frequency [47]. This is theoretically explained using the equation from homogeneous plasma model derived by Godyak [48] as:

$$\frac{P_i}{P_e} = \left(\frac{\omega_p}{\omega_s}\right)^2 \frac{3u_B}{2dv}, \tag{3.14}$$

where $P_i$is the power absorbed by ions, P_e is the electron heating power, ω_s is the driving frequency, d is the plasma half-width, and $u_B = (eT_e/M)^{1/2}$ is the Bohm velocity (M is the ion mass). Another set of results is further obtained by increasing the driven frequency to $f_S = 2$ MHz. As can be seen in Figure 3.14(b), the frequency shift starts for lower biasing voltage at 0.3 V. By increasing the voltage from 0 V to 0.8 V, the plasma density increases with higher driven frequency. The absorption center frequency shifts until it ceases to

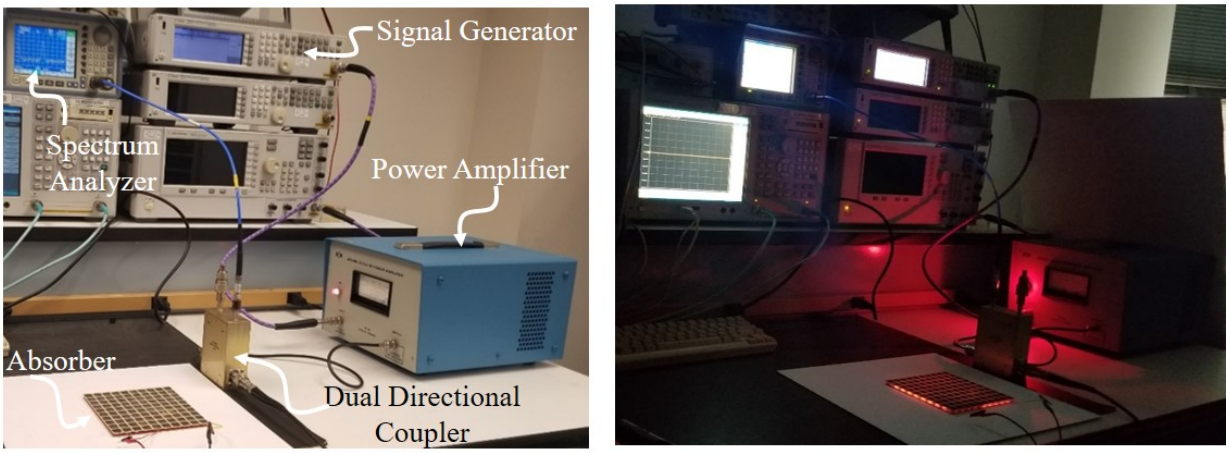

Figure 3.15: Power measurement setup using a high power dual directional coupler and a spectrum analyzer.

increase at around 10.5 GHz. When the voltage is near 0.8 V, the electron density remains virtually unchanged, which is independent of the voltage.

In addition, power consumption of the plasma-shell tuned absorber is estimated by measuring the forward power (P_f) and reflected power (P_r) to and from the plasma-shells, respectively. A dual directional coupler with two auxiliary outputs is used to sample both forward and reflected energy. A 40 dB high power dual directional coupler (C40-110-481/1N by Pulsar Microwave Corp.) is used to characterize the power consumption level of our absorber. The test setups (in Figure 3.15) show the output of the reverse coupling port reduced by the 20 dB attenuator and detected by a spectrum analyzer, while the output of the forward coupling port is terminated by the 50 Ω load. Based on the coupling factor and the attenuation level, the sampled data is used to obtain the reflected power from the load (or absorber). Similarly, by interchanging the role of the forward and reverse coupling port, the forward power is obtained. A summary of the device power consumption analysis for the different driving frequencies is provided in Table 3.3, where P_L is the total power absorbed by the plasma volume and P_u is the power per unit volume. As can be observed from this fidelity test, the percentage of RF power absorbed by the

Table 3.3: Summary of the power distribution at different driven frequencies.

$V_p(V)$	$P_f(W)$	$P_r(W)$		$P_L(W)$		$P_u(W/cm^3)$	
		1 MHz	2 MHz	1MHz	2 MHz	1 MHz	2 MHz
0.3	44.6	26.3	24.4	18.3	20.2	3.81	4.21
0.4	45.7	26.9	25.0	18.8	20.7	3.92	4.31
0.5	47.8	27.9	25.5	19.9	22.3	4.15	4.65
0.6	48.7	28.6	26.2	20.1	22.5	4.19	4.69
0.7	50.6	29.8	27.8	20.8	22.8	4.33	4.75
0.8	52.8	31.1	29.8	21.7	23.0	4.52	4.79
0.9	54.4	33.4	32.3	22.0	23.1	4.58	4.81

plasma increases with the driven frequency. On average, the current biasing setup shows about 42 % efficiency, which can be improved if needed by adding a matching network.

External matching networks between the load (tunable absorber) and the power supply can be designed in order to increase the efficiency of the RF power transfer from the source to the plasma discharge and also reduce the need of higher power for activation voltage threshold. However, a variable matching network may be required since the admittance of the bulk plasma is dependent on the discharge voltage. In fact the admittance of the bulk plasma in Equation (3.10) is a function of the plasma frequency or the electron density of the ionized plasma which is electrically controlled by the applied voltage. All limitations considered, the detailed design and analysis of the biasing network are out of the scope of the material presented in this paper and left for future research items.

Although large-scale plasma-based devices may require a relatively larger amount of power than other electronic tuning mechanisms, this dilemma can be overcome using a high efficiency power amplifier and more matching circuitry. The advantages of our design using plasma technology are highlighted in Table 3.4. Compared with some existing tunable microwave absorbers, superior characteristics of plasma-based devices such as

Table 3.4: Comparison of our plasma-based absorber with other existing tunable absorbers.

Absorber Tuning Mechanism	**Resonant Frequency Tuning range**	**Tuning speed in the order of**	**Thermal effect capability**	**Additional notes**
Varactor diodes [17]	4.35 - 5.85 GHz	nanoseconds	$< 125°C$	Complex biasing networks; design sensitive to polarization.
MEMS [20]	1.12 - 1.32 THz	milliseconds	N/A	Design sensitive to polarization.
Liquid crystal [22]	2.51 - 2.62 THz	milliseconds	$< 300°C$	Not easy to integrate in many applications; design sensitive to polarization.
Graphene [23]	0.91 - 1.08 THz	milliseconds	$< 1500°C$	Complex biasing configuration and not easy to integrate in measurement devices. Also, the realization of graphene using chemical vapor deposition (CVD) is costly.
Liquid metal [25]	0.24 - 0.41 THz	milliseconds	$< 1300°C$	Requires sophisticated control mechanism for synchronous movement of the liquid metal.
Plasma [this work]	9.2 - 10.5 GHz	milliseconds	$< 1000°C$	Can handle high power at microwave frequencies. Simple biasing network and easy integration.

simple biasing schemes, ability to integrate into existing structures to reduce system weight, cost, and most importantly survivability in harsh EM/RF environments (including extreme temperatures and ionizing radiation) outweigh the low power consumption requirement.

4. Plasma-Based Tunable Absorber Loaded with Magneto Dielectric Substrate

4.1 Single pole plasma-based tunable aborber

4.1.1 Design specification

Let us recall that the basis of this project is the investigation of high power handling capability of microwave absorbers that can rapidly adapt to harsh and dynamic EM environments. Although the tuning component (plasma-shells) used in the proposed tunable absorber has the unique property to withstand high power microwave energy [34, 35], the other core material in the design may not be suitable for high-power operation. The proposed absorbers, based on lossy (resistive) layers, may be useful for applications that require moderate power handling and operation in dynamic EM environments. However, although they are relatively low cost and simpler to realize, the lossy resistive layers used to absorb the EM wave have very limited thermal stress capabilities. Usually, these resistive sheets, made of thin-film nickel phosphorous, nickel chromium, nickel chromium aluminum silicon, or chromium silicon monoxide (foils available on Rogers substrates from Ticer and Ohmega Technologies) operate in relatively lower temperature ranges but provide superior absorption bandwidth because of their frequency-independent electrical properties over a broader frequency range. Above their maximum operation temperature, these resistive films are susceptible to burn.

To address this vulnerability, lossy substrates that can withstand higher power EM waves can be used to improve the peak power handling capability of the absorber. In order to account for the total loss provided by the resistive layer in the previous designs, both

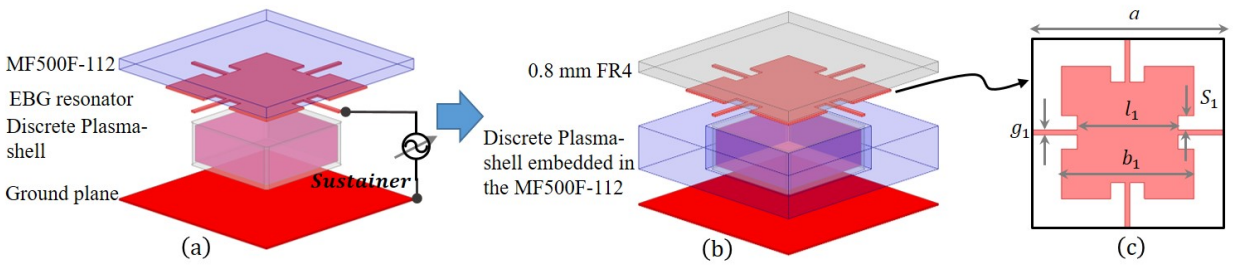

Figure 4.1: (a) Topology of the single pole high power absorber; (b) Modified single pole high power absorber due to practical issues; (c) The physical parameters used to obtain absorption in the C-band are provided: $a = 12.7$; $g_1 = 0.5$; $s_1 = 1.3$; $b_1 = 9.2$; $l_1 = 6.5$ (units in mm).

dielectric and magnetic losses are needed. Unfortunately, such substrate options are limited in today's market in terms of losses and relative power handling capability. Therefore, a systematic design of FSS element shapes with available materials will be required to effectively match the input impedance of the design to the characteristic impedance of free space. In the modified design, a frequency-dispersive lossy magneto-dielectric is used in lieu of the RO4003C used in the previous absorber as shown in Figure 4.1(a). The lossy substrate (Eccosorb MF500F-112 from Laird Technologies) is rigid and can be used for high transient power levels, allowing high temperatures up to 260 °C (500 °F) as mentioned in the datasheet. In order to show that the absorption band of the proposed absorber can be scalable to a desired microwave spectrum, an electromagnetic bandgap (EBG) resonator is employed for the IEEE C-band (4 GHz to 8 GHz) operation. The working principle of the single pole HPM absorber is similar to the previous absorber with the resistive sheet, as the plasma-shells are used to tune the surface impedance of the resonator, which results in a dynamic tuning of the absorption spectral band.

However, this design presents some practical issues for fabrication. The commercially available magneto-dielectrics do not have printed copper layers on any side that could be used to etch the EBG resonator pattern. Moreover, they are available in standard

thickness options (h =3.2 mm, 6.4 mm, 9.5 mm, 12.7 mm, 15.9 mm,19.1 mm, etc.). Printing the EBG resonator on a thin dielectric and pasting the magneto-dielectric directly on top can also lead to a thick design especially for a single pole operation. One way to overcome aforementioned limitations, is to perforate the Eccosorb MF500F substrate (with thickness h = 3.2 mm) in order to accommodate the discrete shells as shown in Figure 4.1(b). The plasma-shell dimensions used in this model are 6 mm × 6 mm × 3 mm. Since the absorber is operating in C-band, the value of the electron collision frequency used to improve the performance of the system is set to be $\nu = 2.0 \times 10^{10}$ rad/s. For fabrication purposes, the value of the gas pressure (P = 100 Torr) can be estimated using Equation (3.12). The magneto-dielectric MF500F-112 is modeled using the "Frequency Dependent Material Setup Option tool" in HFSS. This tool allows one to input all the frequency-dependent data points (real part of permittivity and permeability, the electric loss tangent and magnetic loss tangent) exactly as provided from the material datasheet. HFSS interpolates this data at the desired frequencies during the generation of the solution.

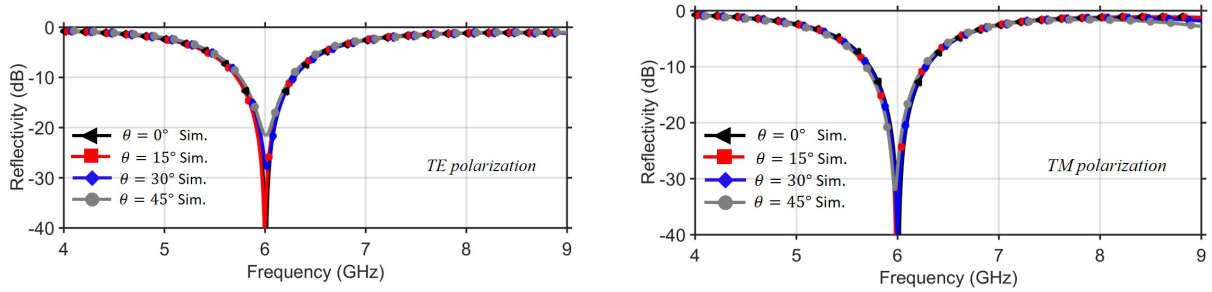

(a) (b)

Figure 4.2: Full wave simulated reflection coefficient of the single pole HPA at various oblique angles of incident wave (a) for TE polarization; (b) TM polarization.

Figure 4.2 shows the full wave simulation results of the HPM absorber performance. At normal incidence angle of the EM wave, results predict about 9 % FBW at 10 dB reflectivity level. The total thickness of the structure is only 4 mm (about $\lambda_0/12$) and the periodicity in the order of $0.25\lambda_0$, where λ_0 is the free space wavelength at 6 GHz. The performance of

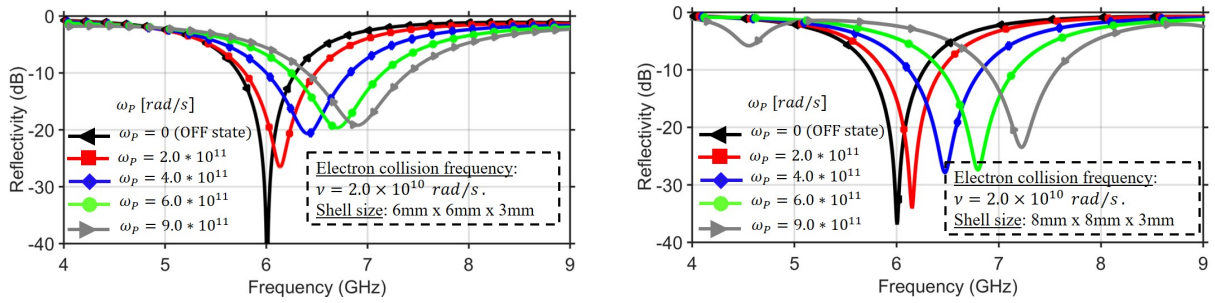

(a) (b)

Figure 4.3: Full wave simulated reflection coefficient of the single pole HPA subjected to different plasma frequencies. Tuning capability observed for the design (a) with shell size: 6 mm × 6 mm × 3 mm; (b) with larger shell size: 8 mm × 8 mm × 3 mm.

the absorber is also investigated across different angles of incidence for both TE and TM polarizations as shown in Figure 4.2. Simulation results predict stable absorption response and at least 20 dB absorption across the absorption band for both TE and TM polarizations when the system is illuminated from various oblique angles ($0° \leq \theta \leq 45°$). The effect of the variation of the plasma frequency ($0 \leq \omega_p \leq 9 \times 10^{11}$ rad/s) on the proposed design performance is also investigated. Simulation results investigating different shell sizes (illustrated in Figure 4.3) show that by changing the value of the plasma frequency within that range, the absorption center frequency increases providing real-time/on-demand electronic tunability of the absorption spectral band. It can also be observed that the larger plasma volume increases the tuning range of the single pole HPM absorber.

4.2 High order plasma-based tunable absorber

4.2.1 Design specification

The proposed design reported in Chapter 3 that incorporates resistive FSS sheets provides broader bandwidth (for the same thickness) compared with the one that incorporates lossy

Table 4.1: Physical dimensions (in mm), electrical thickness, and FBW of various high-order absorbers.

Design	Size	h_M	h_d	a	g	s	l	r	b_1	b_2	b_3	10 dB FBW
2^{nd} order	$\lambda_0/7$	3	0.8	12.5	0.30	1.5	6.5	3.9	9.3	8.2	–	17 %
3^{rd} order	$\lambda_0/4$	3	0.8	12.5	0.15	1.6	6.5	4	9.2	9	7.8	25 %

magneto-dielectric substrate, but its operation service is typically limited to temperatures less than 125 °C. On the other hand, the single pole design that uses lossy substrates with higher thermal conductivity is suitable for higher power microwave energy but the operating bandwidth is limited (9 % fractional bandwidth at 10 dB reflectivity level) by the dielectric and magnetic losses of the MF500F-112 substrate. In order to broaden the absorption bandwidth, a multilayer/multipole design with the ability to have independent tuning control over each resonant frequency is needed.

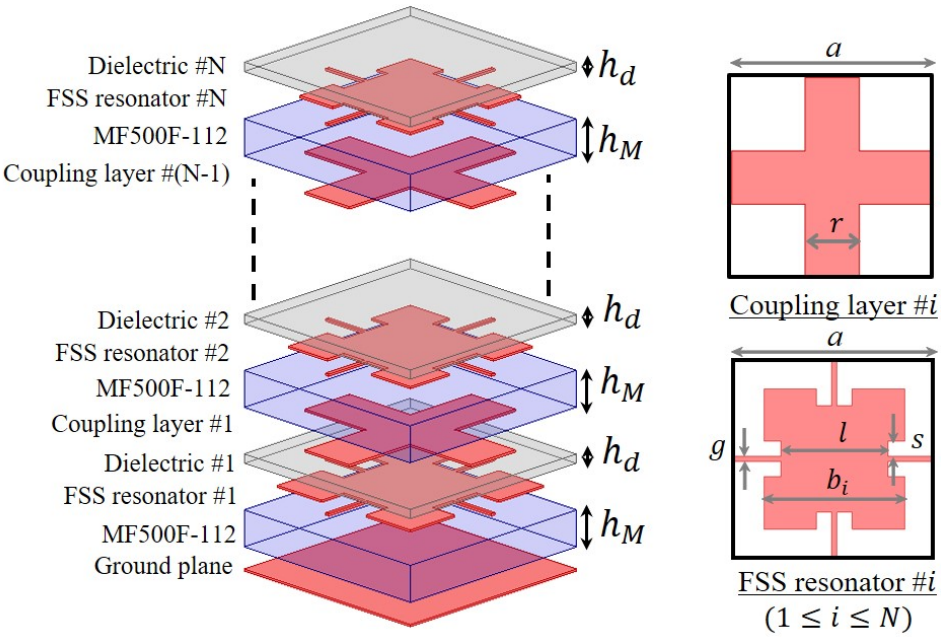

Figure 4.4: Topology of the multipole/high-order ($N \geq 2$) absorber unit cell based on coupling interlayers along with detailed geometry of each layer.

Recently, we have developed a general synthesis for the design of thickness customiz-

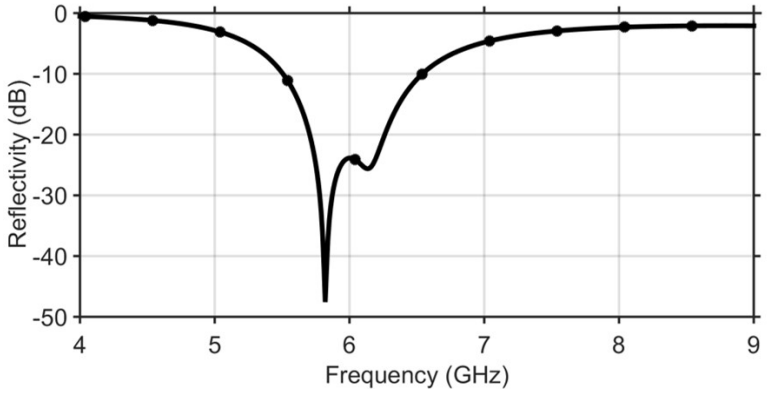

(a)

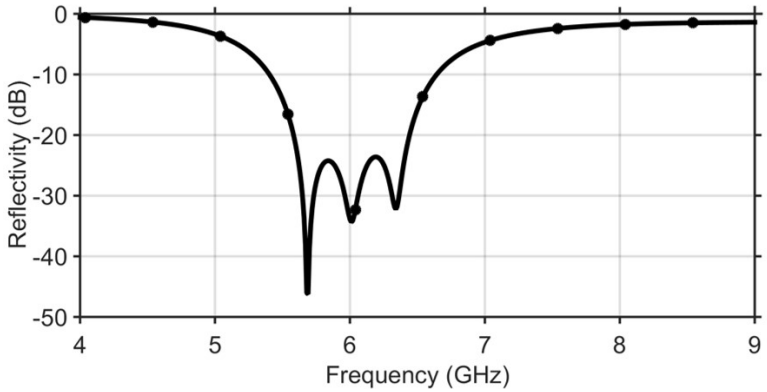

(b)

Figure 4.5: Simulated reflection coefficient of the passive multipole HPM absorbers. (a) Second order response; (b) Third order response.

able high-order bandpass FSSs [31]. The design guide allows simultaneous control of the electromagnetic response and design thickness of multi-layered bandpass FSS filters. The technique is based on coupled bandpass filter theory using admittance inverters (see [31] for more details). The design concept allows the use of readily available commercial dielectric materials with standard thicknesses for multi-layer FSS design technology. Such capabilities also bring practical benefits for tunable metasurfaces by providing flexibility in integrating tuning elements or materials that require precise control of physical dimensions [39]. The proposed multipole absorber relies on the design concept we presented in [31]. A high-order ($N \geq 2$) bandpass FSS using such technique is placed above a ground plane as

depicted in Figure 4.4. For such combinations, the absorption band is mainly determined by the operation frequency of the FSS and loss can be introduced in the design using either resistive FSS elements or lossy substrates. The latter is taken into account, and lossy substrates, consisting of Eccosorb MF500F series materials (with thickness h_M) are used to absorb the EM wave energy. The FSS is formed by a periodic array of cascaded EBG resonators that behave as a parallel LC bandpass filter. An interlayer consisting of a mesh grid is placed between the resonators to regulate the coupling level between consecutive resonators for various separations. The metallic layers are printed on FR4 dielectrics with thickness h_d. The proposed N^{th} order multipole absorber is comprised of the ground plane, N metallic bandpass resonators, N Eccosorb MF500F lossy substrates, N dielectrics slabs and $(N-1)$ coupling interlayers. A second ($N=2$) and third ($N=3$) order response are implemented to obtain absorption in the C-band. The physical dimensions of the higher order absorbers along with response characteristics are summarized in Table 4.1. The simulated full wave EM results illustrated in Figure 4.5 predict absorption of the EM wave in the C-band centered at 6 GHz with 17 % and 25 % fractional bandwidth (FBW) at 10 dB reflectivity level for the second and third order absorbers, respectively. The total thickness of the two-pole absorber is 8 mm (about $\lambda_0/7$) and the periodicity in the order of $0.25\lambda_0$, where λ_0 is the free space wavelength at 6 GHz. For the three-pole absorber the total thickness is 12 mm (about $\lambda_0/4$) with a the periodicity in the order of $0.25\lambda_0$. In addition to the reduction of the RCS provided by these multipole frequency selective absorbers, the skirt selectivity of the absorption band with high out of band reflection can be beneficial for other applications. In fact, the high reflectivity obtained outside the absorption band is relevant in the realization of dual-band reflector antennas [49] for satellite communication.

To demonstrate the absorber capability in adapting to various design thicknesses, the response of the two-pole absorber is obtained for different values of the MF500F-112 thickness h_M (2 mm, 3 mm and 4 mm). The physical dimensions of the absorber for

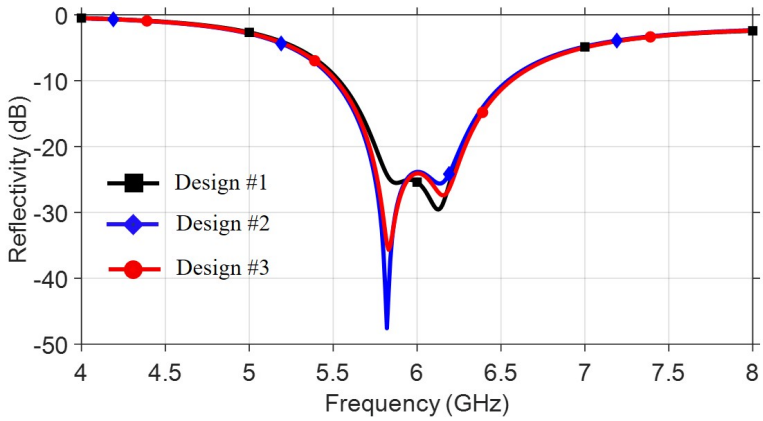

Figure 4.6: Simulated reflection coefficient of the passive absorber with three different customized thicknesses.

Table 4.2: Physical dimensions (in mm), electrical thickness, and FBW of the three design configurations with second order response ($N = 2$).

Design	Size	h_M	h_d	a	g	s	l	r	b_1	b_2	10 dB FBW
#1 (2^{nd} order)	$\lambda_0/9$	2	0.8	12.5	0.17	1.56	6.5	3.6	9.3	8.3	17 %
#2 (2^{nd} order)	$\lambda_0/7$	3	0.8	12.5	0.30	1.50	6.5	3.9	9.3	8.2	17 %
#3 (2^{nd} order)	$\lambda_0/5$	4	0.8	12.5	0.35	1.47	6.5	4.2	9.3	8.2	17 %

each configuration without the plasma-shells are summarized in Table 4.2. As shown in Figure 4.6, all three design configurations provide virtually the same absorption response. The results show a second order response of about 17 % fractional bandwidth at 10 dB reflectivity level.

In order to add the reconfigurability feature to the multipole absorber, cuboid cavities are created within the lossy magneto-dielectric substrate, thereby allowing the hollow ceramic gas-encapsulating chambers (plasma-shells) to be embedded in the design as shown in Figure 4.7. The shells (size: 6 mm $\times$ 6 mm $\times$ 3.3 mm) are filled with 0.1 % Argon - 99.9 % Neon at 100 Torr of pressure with the electron collision frequency value set to: $\nu = 2.0 \times 10^{10}$ rad/s. RO4003C, a hydrocarbon ceramic laminate from Rogers Corporation's RO4000 series (which are known for their reliability when subjected to severe thermal

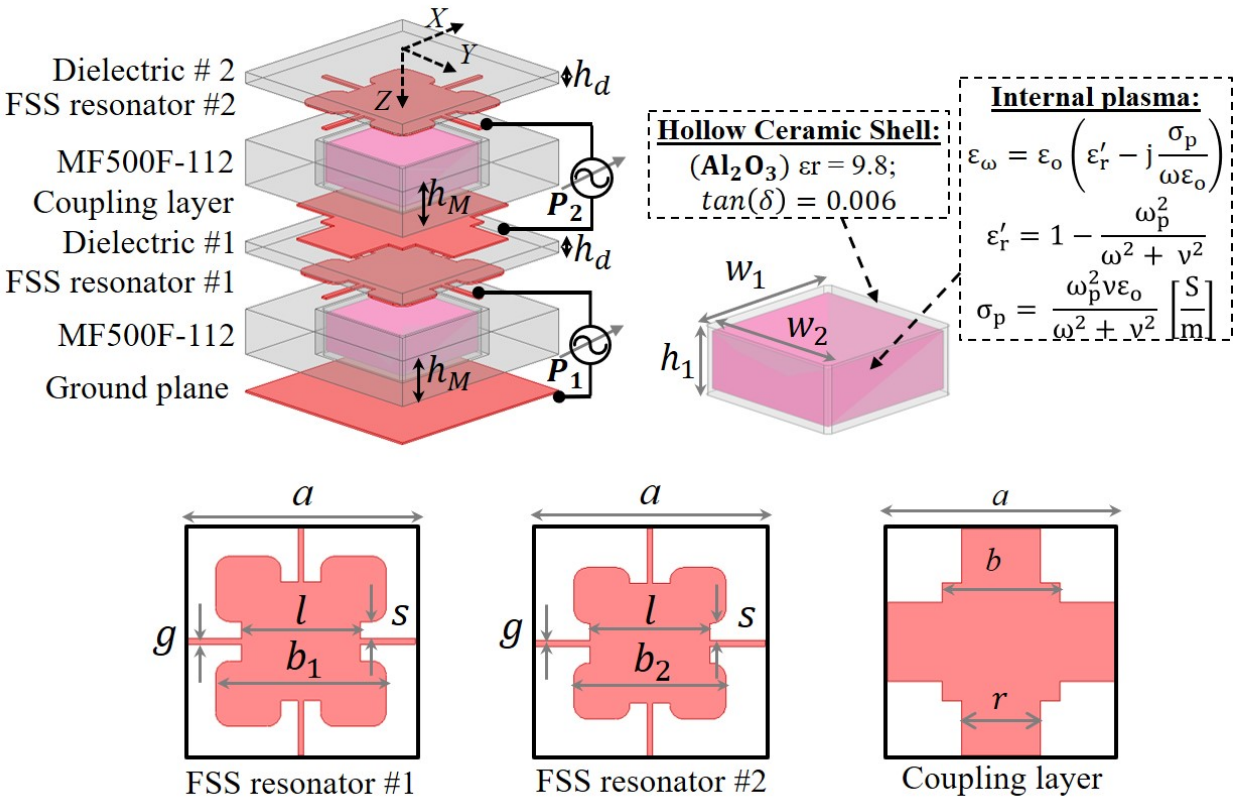

Figure 4.7: Proposed unit cells of the two-pole tunable plasma-based absorber based on coupling interlayers. The physical parameters used to obtain absorption in the C-band are provided: $h_M = 3.5$; $h_d = 1.524$; $a = 10$; $g = 0.4$; $s = 1.65$; $b_1 = 9.4$; $b_2 = 8.66$; $l = 6.5$; $b = 6.5$; $w_1 = w_2 = 6$; $r = 3.6$ (units in mm)

shocks) is used for the dielectrics layers[1]. In the active layer, both the resonators and the coupling interlayers are used as biasing surfaces for the shells. In order to minimize field enhancement at the sharp corners of the resonators, a fillet of radius 0.7 mm is added at the corner of the resonators patch. The physical parameters of the active absorber are provided in Figure 4.7. Simulation results shown in Figure 4.8 predict stable absorption response across the absorption band for both TE and TM polarizations when the system is illuminated from various oblique angles ($0° \leq \theta \leq 60°$). However, above 40° angle of

[1]For better thermal management, a higher temperature material RO4003C is used in this Final Report as substitute for the FR4 dielectrics that was used in the previous Report.

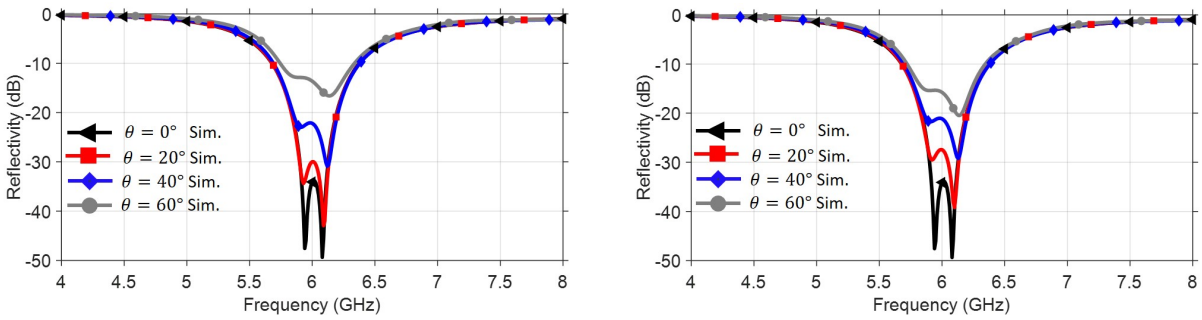

Figure 4.8: Full wave simulated reflection coefficient of the multilayer absorber at OFF state for various oblique angles of incident wave. (a) TE polarization. (b) TM polarization.

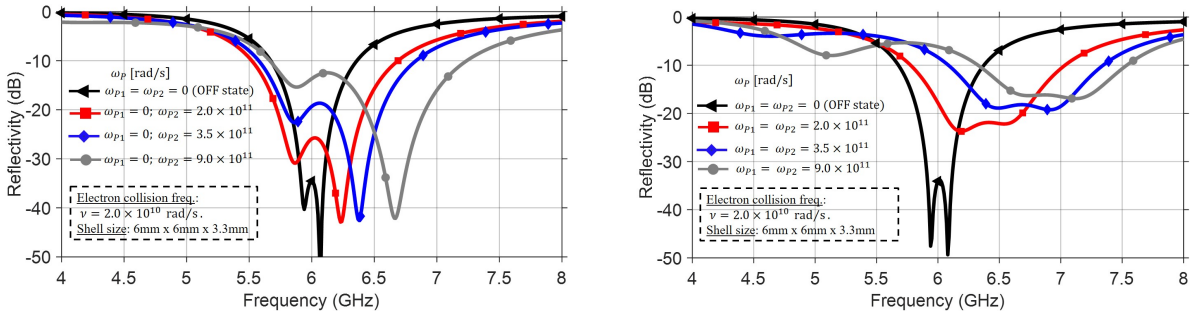

Figure 4.9: Full wave simulated reflection coefficient of the multilayer absorber at ON state subject to different plasma frequencies. Tuning capability observed for (a) Only the top plasma layer is activated and (b) Both plasma layers are activated.

incidence, the reflectivity of the absorber has increased to above −20 dB.

The variation of the biasing voltage is mimicked by applying different plasma frequencies through simulation. On one hand, we assume that only the top plasma layer is excited ($\omega_{P1} = 0$). The variation of the plasma frequency ($0 \leq \omega_{P2} \leq 9 \times 10^{11}$ rad/s) predicts a tuning of the absorption spectrum and rate. The higher absorption resonant frequency has shifted from 6.2 GHz to 6.7 GHz (see Figure 4.9(a)). However, the wider absorption band is obtained at the expense of the absorption rate. On the other hand, when both plasma layers are excited, the effect of the variation of both plasma frequencies such that $\omega_{P1} = \omega_{P2}$ (see Figure 4.9(b)) predicts a tuning of both resonant frequencies across the

C-band. It can be seen that the center frequency shifts to higher frequency (from 6 GHz to 7 GHz).

4.2.2 Fabrication processes and measurement results

The proposed multilayer plasma-based tunable absorber is fabricated and tested in a free space environment to validate the numerical results. The metallic resonators and coupling layer are patterned on the Rogers substrate using a wet etching process. Also, the magneto-dielectric MF500F-112 substrates are finely drilled and perforated using a milling machine (LPKF ProtoMat S103) as shown in Figure 4.10. The prototype board is an array of 13×13 elements, printed on the Rogers substrate with a total size of $130\,\text{mm} \times 130\,\text{mm}$.

First, a pre-test is performed to evaluate the performance of the absorber without the plasma shells. A frame made out of thermoplastic material using a 3D printer (Monoprice Maker Select v2) is used for fine alignment and to hold the layers together. A small aperture of the size of the absorber is carved out at the center of a commercially available large metal-backed foam broadband absorber (Eccosorb AN-75) to mount the DUT as shown in Figure 4.11. The Eccosorb AN-75 frame is used to reduce diffraction effects from the edges of the DUT. The calibration procedure is the same as previously described in

Figure 4.10: Fabricated perforated lossy magneto-dielectric (MF500F-112)

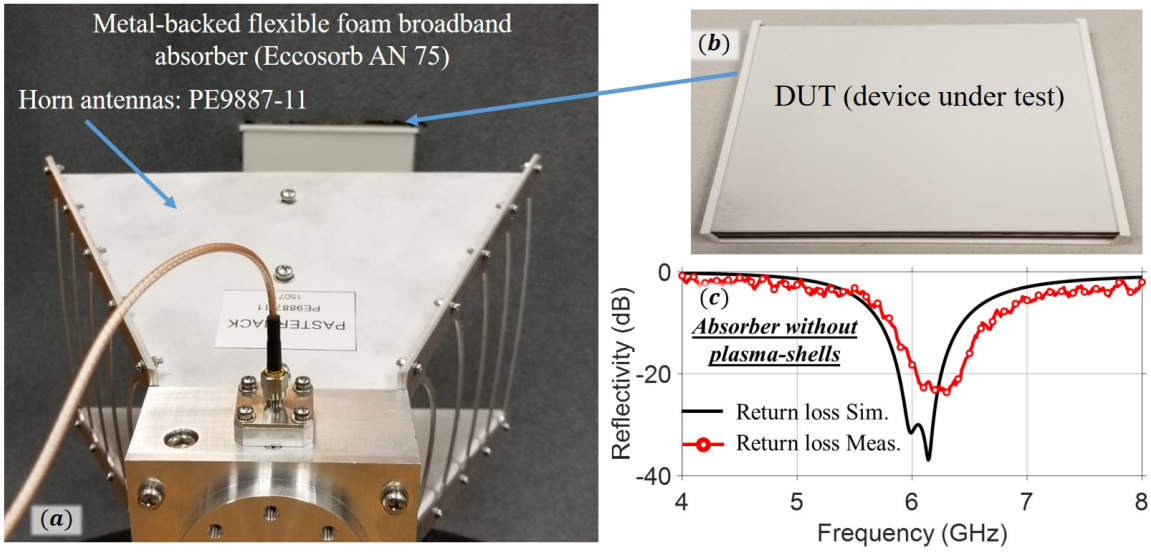

Figure 4.11: (a) Photograph of the test setup (free space); (b) Fabricated prototype (without the plasma-shells) inside a 3D printed frame; (c) Measurement vs simulated result of the absorber without plasma-shells.

[50]. The measured return loss of the absorber without plasma-shells compared to its counterpart simulated result is illustrated in Figure 4.11. The results predict a second order response of about 14% fractional bandwidth at 10 dB reflectivity level. The link between simulated and measured results shows that the MF500F-112 magneto-dielectrics have been accurately modeled in the simulation tool. A slight contrast between both results can be due to the small size of the prototype and the material tolerances. The plasma-shells used for this experiment are commercially available from Imaging Systems Technology Inc. The shells are filled with 0.1 % Argon - 99.9 % Neon mixture at 100 Torr gas pressure. The gas pressure is estimated from the electron collision frequency ($\nu = 2.0 \times 10^{10}$ rad/s) by solving Equation (3.12), the theoretical expression for neon gas derived in [46] at 300 K electron temperature. The fabrication procedure of the multilayer absorber with the plasma shells embedded in the lossy perforated magneto-dielectric substrates MF500F-112 is as follows: (a) the shells are hand-placed in the perforated lossy magneto-dielectric (MF500F-112) backed by the ground conductor; (b) conductive silver epoxy is deposited on the top

side of the shells using a syringe; (c) the bottom plasma excitation layer is added on top of the lossy magneto-dielectric; (d) the second perforated lossy magneto-dielectric is added on top of the bottom plasma excitation layer; (e) shells with epoxy deposited on both top and bottom side are hand-placed in the substrate chambers; (f) the top plasma excitation layer is added on top of the lossy magneto-dielectric. The stacked-up prototype is shown in Figure 4.12. The performance of the absorber (at OFF state) across different angles of incidence for both TE and TM polarizations is experimentally obtained. Measured results Figure 4.13 show acceptable and stable reflection response when the system is illuminated from various oblique angles ($0^\circ \leq \theta \leq 60^\circ$). Both the measured results (Figure 4.13) and simulated results (Figure 4.8) demonstrate acceptable agreement although the measured center frequency has shifted to 6.1 GHz.

Figure 4.12: Photograph of the stacked-up multilayer absorber (with the plasma-shells embedded within the lossy magneto-dielectric) inside the 3D printed frame.

In order to turn the device ON, a class A, RF power amplifier (ENI 2100L with 50 dB nominal gain and operating frequency ranging from 10 kHz to 12 MHz) is used to sustain the plasma layers. The RF power amplifier (PA) amplifies a sinusoidal wave produced by Keysight's N5181A MXG RF analog signal generator operating at 2 MHz. The output of the PA is then connected to the bias traces of the absorber via a coaxial cable. By monitoring the power level of the CW through the PA front panel meter and changing the voltage from the signal generator, different voltage is supplied to the plasma volume. The excited

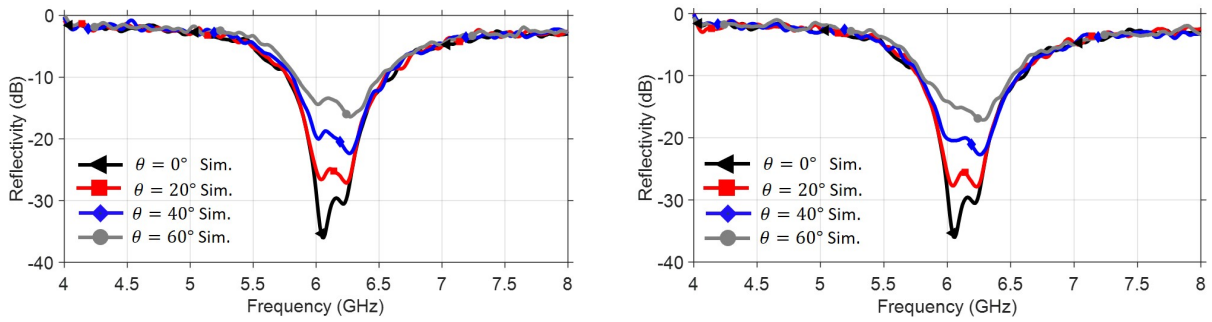

Figure 4.13: Measured reflection coefficient of the multilayer absorber at OFF state for various oblique angles of incident wave. (a) TE polarization. (b) TM polarization.

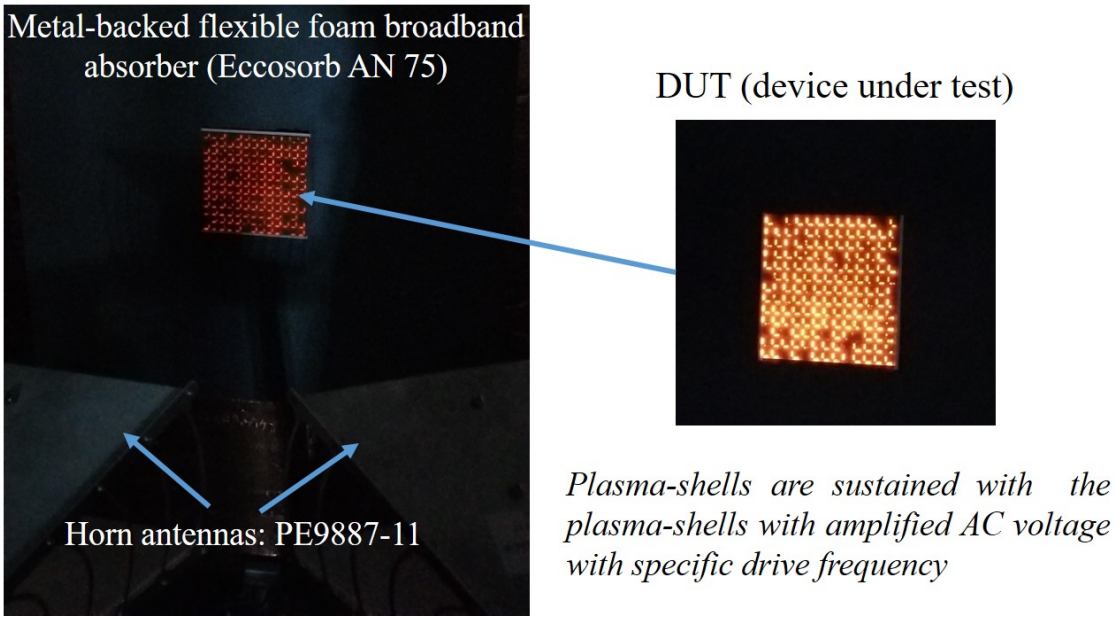

Figure 4.14: Photograph of the test setup (free space) when the absorber is excited with various RF powers.

DUT is shown in Figure 4.14. When the top plasma layer is only excited with various RF power such that $P_1 = 0$ and $0 \leq P_2 \leq 70\,\mathrm{W}$, the measured results at normal angle of incidence indicate a tuning of the higher absorption resonant frequency (see Figure 4.15(a)). However, when both plasma layers are activated ($0 \leq P_1 = P_2 \leq 70\,\mathrm{W}$), a tuning of the absorption spectrum range is perceived (see Figure 4.15(b)) showing a shift of the

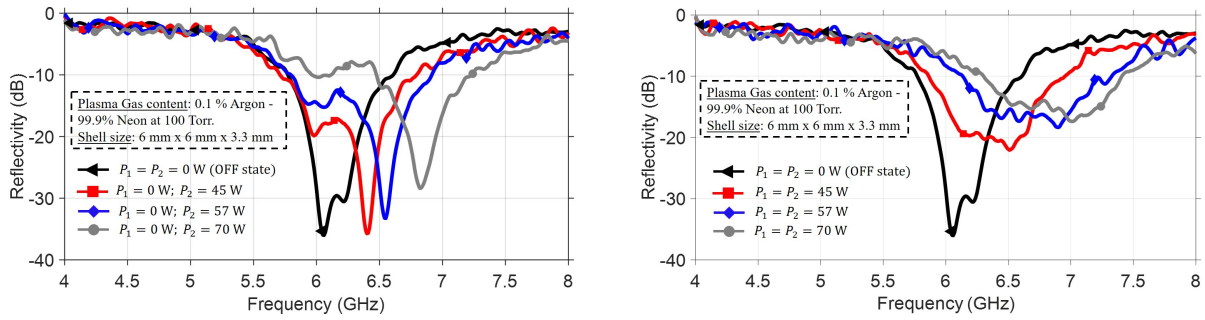

Figure 4.15: Measured reflection coefficient of the multilayer absorber at ON state. The plasma volume are excited independently excited with various RF power intensities. Tuning capability observed for (a) Only the top plasma layer is activated and (b) Both plasma layers are activated.

absorption center frequency. These experimental results validate the fact that the proposed absorber, when properly biased, allows real time tuning of the operating bandwidth, thus can be adapted to a dynamic EM environment.

5. Multiphysics Analysis of Two-Pole High Power Microwave absorber

Multiphysics analysis is a powerful design process that can be used to understand multiple physical phenomena of electromagnetic devices under real world conditions. Such analysis, composed of EM simulation coupled with thermal, structural, and/or fluidic simulations [51, 52] are critical for the design liability associated with performance and cost. One of the real world applications of multiphysics analysis involves the impact of high power electromagnetic interference with electronics devices. In such events, researchers have focused their understanding on electronic attacks and electronic protection. These inquiries have led to tremendous development capabilities that are evolving rapidly with modern technology [53–55]. Advanced countermeasures electronic systems, such as electronic coating shielding, isolators, filter limiters, frequency selective surfaces, microwave absorbers [39, 50, 56–61], etc., have been explored to ensure functional safety of EM devices. Conversely, techniques such as electronic jamming and deception, anti-radiation weapons, use of HPM and EMP weapons [62–68] are often exploited to target those protective layers and damage the electronic and electric systems through EM coupling. The exposure of electronic systems to high power level EM interference, whether it is intentional or not, can disrupt their performance and cause device failure depending on the core material and the microscopic features of the systems architecture. Usually, the electric fields induced in the system caused by the incident wave are associated with current and voltage surges that can initiate electromagnetic breakdown, arcing, or overheating of the system [69]. Under such conditions, design specifications such as EM-thermal-mechanical management can no longer be neglected. The ANSYS multiphysics simulator has proven to be a reliable and powerful software package for the study of EM-thermal-mechanical coupling [70, 71].

While the EM analysis is performed by ANSYS HFSS, both thermal analysis and stress analysis can be performed using ANSYS Mechanical. For instance, if the electronic system is lossy, the electric fields calculated from Maxwell's equations are used to compute the power dissipated in the system. The EM losses (surface and volume loss densities) are then converted into heat using heat transfer equations. Then, the temperature distribution can be utilized to analyze the thermal stress (expansion or contraction). The deformation caused by the thermal stresses and the change in temperature are fed back into HFSS and will affect the electro-thermal properties of the materials. This cycle is repeated until the temperature reaches its steady state. The interaction between EM and heat transfer using both ANSYS HFSS and ANSYS Mechanical provides an accurate and complete bidirectionally coupled physics analysis. In this section, the physical limitation of a plasma-based tunable conductor-backed absorber under high power microwave levels is demonstrated using multiphysics numerical analysis. The peak power (for a very short duration pulse) and average microwave power (for a continuous wave) handling capability of the active absorber have been investigated. The numerical analysis is carried out to predict the dielectric and air breakdown levels within the system. Also, since the absorber converts the EM energy into thermal energy, the EM wave and heat transfer are coupled together to evaluate the thermal behavior of the absorber. Both the steady state and transient state analyses are performed when the device is exposed to various incident power densities. A non-uniform temperature distribution is obtained with hotter spot located within the lossy magneto-dielectric. Since testing at high power microwave levels is potentially unsafe, experiments are performed with relatively moderate far-field power densities to validate numerical results. The temperature distributions on the top surface of the absorber are obtained using a thermal imaging infrared camera (FLIR E6).

5.1 Physical impact of high power microwave source on the proposed multilayers absorber

High peak and average microwave power sources present severe challenges for the reliability and safety of resonant structures. Under exposure of high-power RF, the physical interaction between the EM field and the electronic system on a molecular level must be investigated. Electromagnetic breakdown and overheating of the device are feasible causes of design failure. In general, EM breakdown events are the primary concerns associated with very short pulse durations (in terms of μs) of high peak power. This happens when the induced electric field within the device becomes greater than the breakdown limit of air or dielectric. In our resonant absorber, the slots within the metallic layers enhance the localized electric field intensity from a buildup of negative and positive charges. As a result of the electric discharge, current will flow through the dielectric to create a short circuit as the insulating material becomes a good conductor. On the other hand, overheating of the system is associated with high average power with sustained continuous wave. The energy dissipated in the system due to the time averaged metallic and dielectric losses is converted into heat, which can become problematic depending on the selected design materials.

5.1.1 Estimation of the absorber breakdown threshold

The prediction of the absorber electrical breakdown level is a very complex task because the discharge process is transient and occurs on a microscopic level. While many factors can cause microwave-metal electrical discharge mechanism, we exploit the effect of the field enhancement caused by high peak microwave power. Numerically, the dielectric and air breakdown level within the absorber can be estimated by quantifying the maximum

field enhancement factor (MFEF) [72]. MFEF is defined as the ratio between the maximum local electric field intensity inside the system and the electric field intensity of the incident EM wave. Therefore, a microwave system resilient to high power RF is expected to have lower MFEF.

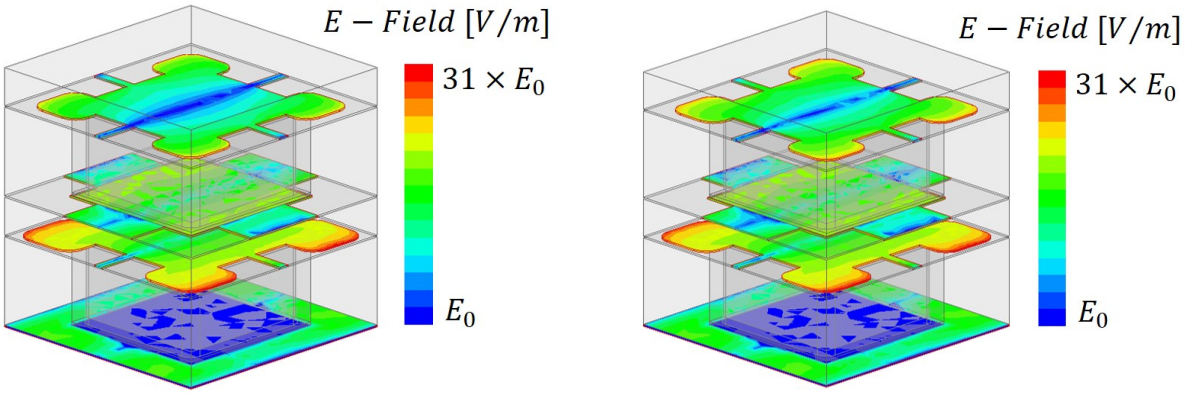

Figure 5.1: Simulated E-field distribution in the metallic layers at a unit cell level of the absorber illuminated with an incident power of 1 W. The electric field with intensity E_0 = 2746 V/m is coupled to the absorber. The induced field distribution is observed at (a) the first resonant frequency f_1= 5.9 GHz and (b) the second resonant frequency f_2= 6.1 GHz

However, at resonance the fields inside small metallic gaps are maximally enhanced. The electric field distribution in the metallic layers of the absorber unit cell is numerically obtained at both resonance frequencies f_1 = 5.9 GHz and f_2 = 6.1 GHz. When the cross section of the unit cell (with periodicity a = 10 mm) is illuminated with an incident power of 1 W, a maximum incident power density of 10 000 W/m^2 which is equivalent to an electric field intensity of E_0 = 2746 V/m is coupled to the system.

The results shown in Figure 5.1 predict strong local field enhancement at both EBG resonators. It can be seen that, the field is strongly enhanced at the edges of the metallic layers. The MFEF of the absorber (without/with resonator corners filleted) is extracted across the C-band (4 GHz to 8 GHz) using full-wave EM simulation and the result is

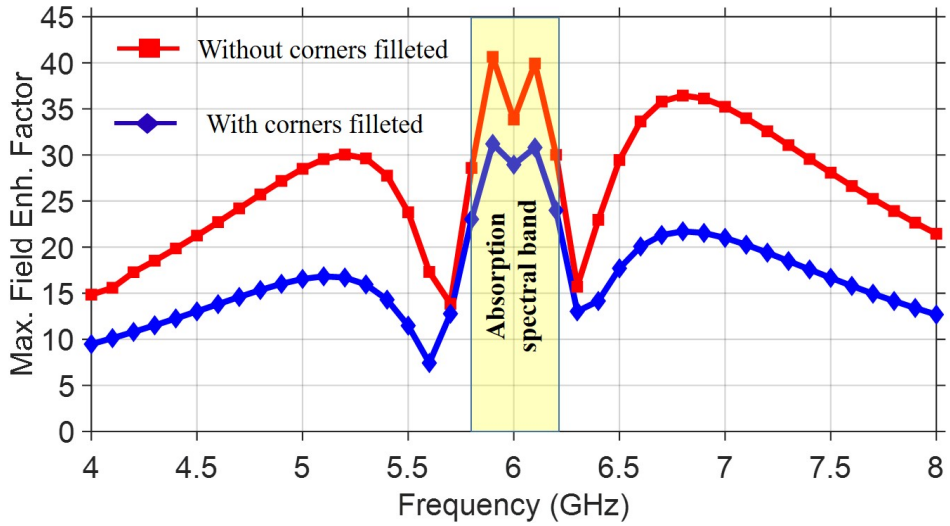

Figure 5.2: Extracted MFEF values at different frequencies of the absorber without and with filleted resonators corners.

Table 5.1: Approximated maximum allowed power density (in MW/m^2) for very short pulse duration of high power.

Design	5.8 GHz	5.9 GHz	6.0 GHz	6.1 GHz	6.2 GHz
Without filleted resonator corners	14.5	7.2	10.4	7.5	13.2
With filleted resonator corners	22.5	12.3	14.2	12.5	20.7

depicted in Figure 5.2. It is perceived that the proposed design with filleted resonators corners show slightly better performance in handling higher microwave power. The value of the MFEF is higher in the operation band of the absorber (with maximum value = 31) observed at both resonant frequencies for the proposed design. At OFF state, the air gap existing in the cavity is the most limiting medium with electrical breakdown strength E_B = 3 MV/m. For very short pulse duration of high peak power, the maximal power density the absorber can withstand at specific frequencies is depicted in Table 5.1. Overall, the data obtained showed the maximum allowed incident power density is about S =12.3 MW/m^2 for the proposed multilayer absorber at OFF state.

5.1.2 Thermal analysis of the proposed multilayer absorber

As mentioned previously, when the absorber is coupled with a high average power CW, thermal analysis needs to be taken into account to avoid design failure due to material heating and possible burning. Therefore, it is important to understand how the material choice can affect the thermal and electrical performance of the design. The CW incident power density allowed by the design can be obtained based on the thermal limit of their temperature dependent materials. A comprehensive multiphysics solution that couples full-wave EM to thermal analysis is performed using HFSS and Icepak from ANSYS.

Table 5.2: Thermal properties of the absorber materials.

Material	Thermal conductivity ($W.m^{-1}.K^{-1}$)	Density ($Kg.m^{-3}$)	Specific heat ($J.Kg^{-1}.K^{-1}$)	Operating temperature limit (°C)
Copper	401	8933	356	< 750
Alumina	27	3970	910	< 1750
Neon	0.0498	0.1079	1029.9	< 1000
Rogers RO4003C	0.71	1700	900	< 280
MF500F-112	1.44	3250	1300	< 260

In general, the temperature dependency of the materials' electrical properties (such as dielectric constant, loss tangent, conductivity) are governed using a quadratic approximated equation [73]:

$$x(T) = x(T_0)\left[1 + C_1(T - T_0) + C_2(T - T_0)^2\right]. \tag{5.1}$$

where T_0 is the initial temperature, T is the temperature of the heated material (which can be position dependent as well), and C_1 and C_2 are the linear and quadratic expansion coefficients, respectively. A bidirectionally coupled analysis is possible if the temperature dependency of all the materials electrical properties are known. In such case, the transient

frequency response of the design due to temperature drift and structural deformation can be also obtained. However, in this section our analysis focuses on the heat generated solely due to Joule heating within the absorber for different incident power densities.

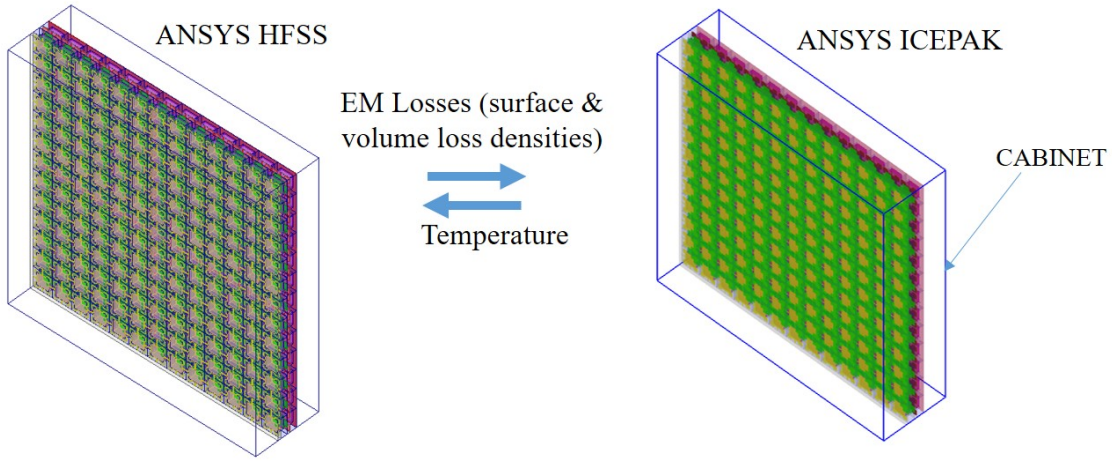

Figure 5.3: Simulation model of the finite size multilayer absorber illustrating the coupling between ANSYS HFSS and ICEPAK.

The thermal specification of the design modeled in Icepak is illustrated in Table 5.2. These values are taken under ordinary conditions and it can be seen that the magneto-dielectric MF500F-112 is the limiting material in terms of the maximum operating temperature ($<$260 °C). Beyond this threshold, known as the glass transition temperature (T_g), the hard polymer will become soft and lose its electrical and mechanical integrity. The simulation set up in Icepak is performed in a natural convection environment (heat transfer coefficient $HTC = 10\,\mathrm{W \cdot K^{-1} \cdot m^{-2}}$), with the radiation ON (for heat transfer) and ambient external temperature. In order to predict the temperature profile of the design, the exact finite size of the absorber is taken into account (as shown in Figure 5.3) to consider the edge effects, although a heavy simulation CPU time is required.

Both the steady and transient state simulation results are obtained when the absorber is exposed to a continuous plane wave. The steady state temperature profile of the absorber exposed to various power densities at the center frequency $f_0 = 6.0\,\mathrm{GHz}$ is

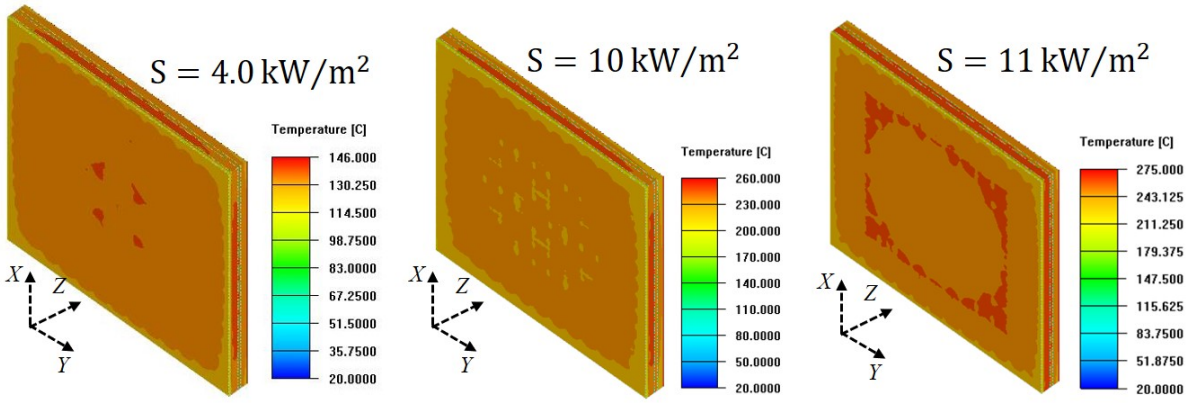

Figure 5.4: Simulated steady state temperature map throughout the multilayer absorber exposed to various power densities with incident plane wave at f_0 = 6.0 GHz.

Table 5.3: Simulated maximum temperature (°C) within the MF500F-112 substrates for different power densities across the absorption spectral band.

Power density	5.8 GHz	5.9 GHz	6.0 GHz	6.1 GHz	6.2 GHz
S =4.0 kW/m^2	145	145.7	146	145.8	146
S =10 kW/m^2	261	259.5	260	261	260.5
S =11 kW/m^2	275.4	274.8	275	275	274.6

illustrated in Figure 5.4 (which reflect the temperature plot in both substrates and metallic surfaces). It appears that a non-uniform spatial temperature distribution is obtained such that the peak temperature is located within the magneto-dielectric MF500F-112, where the substrate losses are the most significant. A report of the simulated maximum temperature generated within the MF500F-112 substrate for different power densities across the absorption spectral band is summarized in Table 5.3. It can be seen that the temperature increases with the power density. A transient simulation is also performed on the multilayer absorber. The 3D temperature distribution throughout the absorber is obtained within one-hour time frame for various power density at the center frequency as shown in Figure 5.5. The initial temperature of the absorber is set to the room temperature

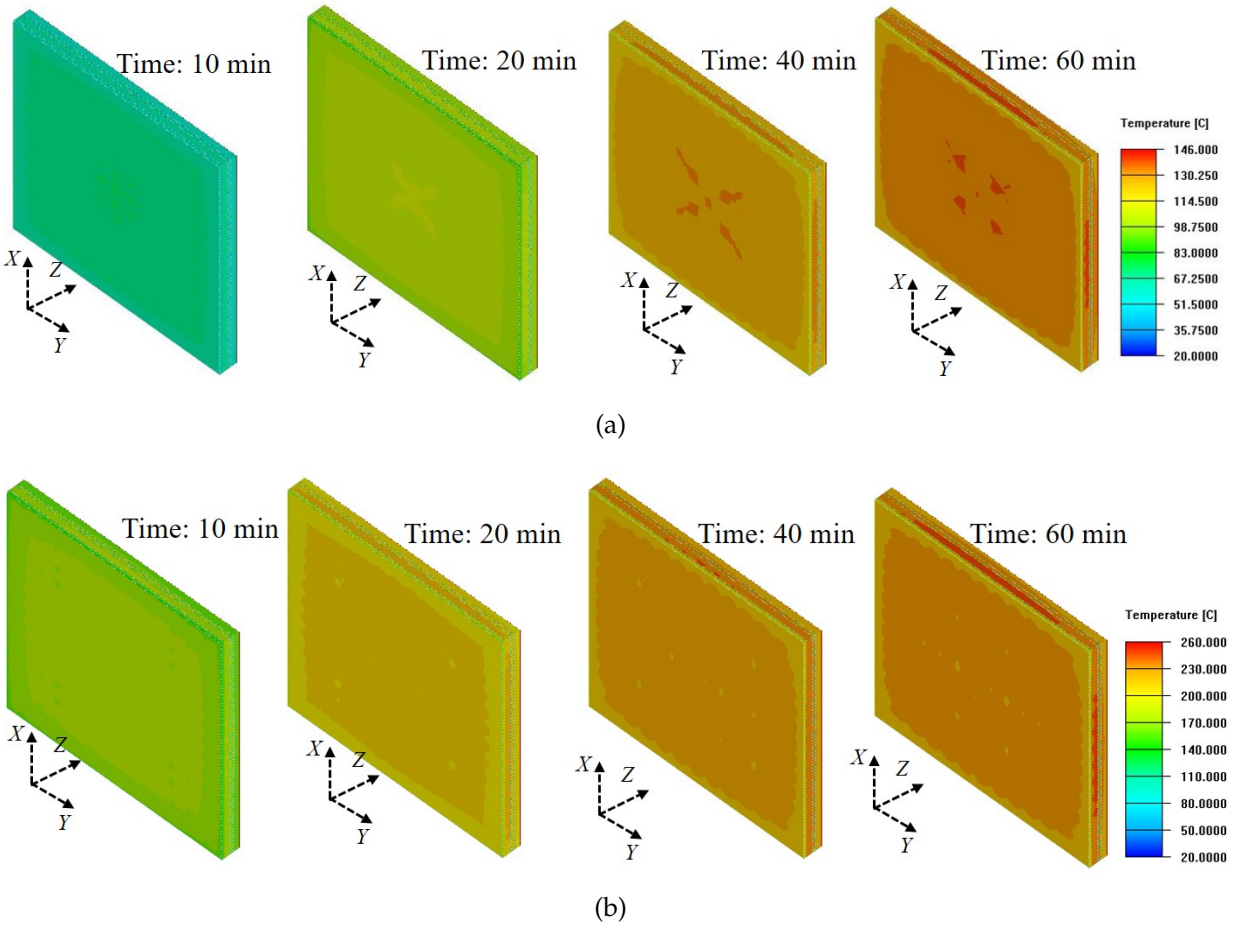

Figure 5.5: Simulated transient state temperature map throughout the multilayer absorber with incident plane EM wave at f_0 = 6.0 GHz. The absorber is exposed to various power densities. (a) S =4.0 kW/m^2; (b) S =10 kW/m^2.

(T_0 = 20 °C). The transient simulated results shows that the temperature within the absorber increases with time and converges to the steady state after one hour. The plot in Figure 5.6 (maximum temperature versus time) is provided to illustrate the trend of the temperature increase over time within the Rogers RO4003C and the MF500F magneto-dielectrics. It is observed that the temperature rises quickly for higher incident power densities. Based on the data projected, the maximum average power density the absorber can tolerate at OFF state for an incident CW is about S_A =10 kW/m^2.

However, the question remains if the average power handling capability of the absorber

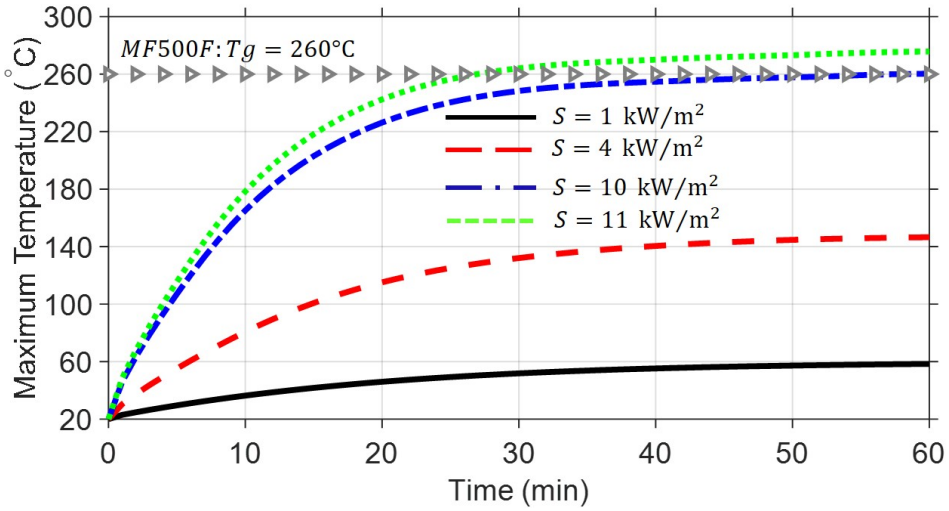

Figure 5.6: Time variant simulated peak temperature plot at OFF state throughout the MF500F-112 substrates illustrated for various power densities with incident plane EM wave at $f_0 = 6.0\,\text{GHz}$.

Table 5.4: Four different tuning states of the the plasma along with their respective plasma frequencies and absorption center frequencies.

Tuning state	Plasma frequency: ω_p [rad/s]	Absorption center frequency: f_c [GHz]
OFF State	0	6.0
ON State #1	2.0×10^{11}	6.4
ON State #2	3.5×10^{11}	6.7
ON State #3	9.0×10^{11}	6.9

obtained at OFF state is still valid for all the plasma tuning states. Theoretically, at ON state when the plasma frequency ω_p increases, its inductance value as modeled in Section 3 ($L_p = \omega_p^{-2} C_0^{-1}$) decreases, as well as its resistance value ($R_P = \nu L_p$). The change in the plasma resistance can affect the temperature generated from energy dissipated through Joule effect. Therefore, it is possible that the radiation of the plasma electron temperature through heat transfer can alter the temperature distribution of the absorber under high power continuous wave excitation at ON state. To demonstrate this ambiguity, even though the transition between tuning states are not abrupt, the distribution of the volume

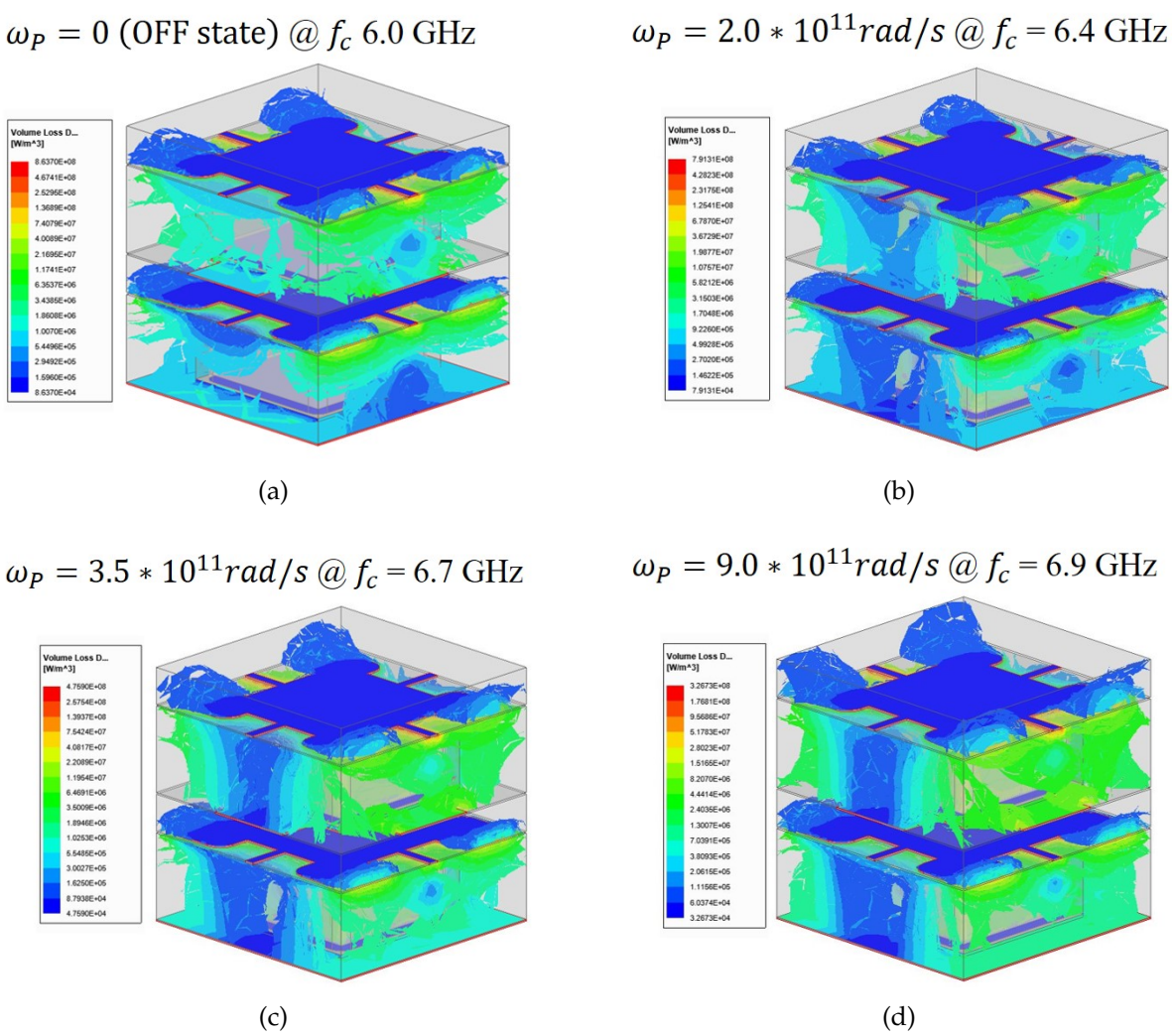

Figure 5.7: Simulated volume power loss density in a unit cell of the multilayer absorber exposed to an incident power of 1 W. (a) OFF state; (b) ON State #1; (c) ON State #2; (d) ON State #3.

power loss density within the multilayer absorber is investigated for the discrete tuning states of the plasma shown in (see Figure 4.9(b). The description of these tuning states are illustrated in Table 5.4 where each plasma state is associated with their respective plasma frequency and absorption center frequency. When the absorber unit cell is illuminated with an incident power of 1 W, simulated results in Figure 5.7 predict that the dissipated power is localized in the substrates producing a nonuniform spatial distribution. It can be seen

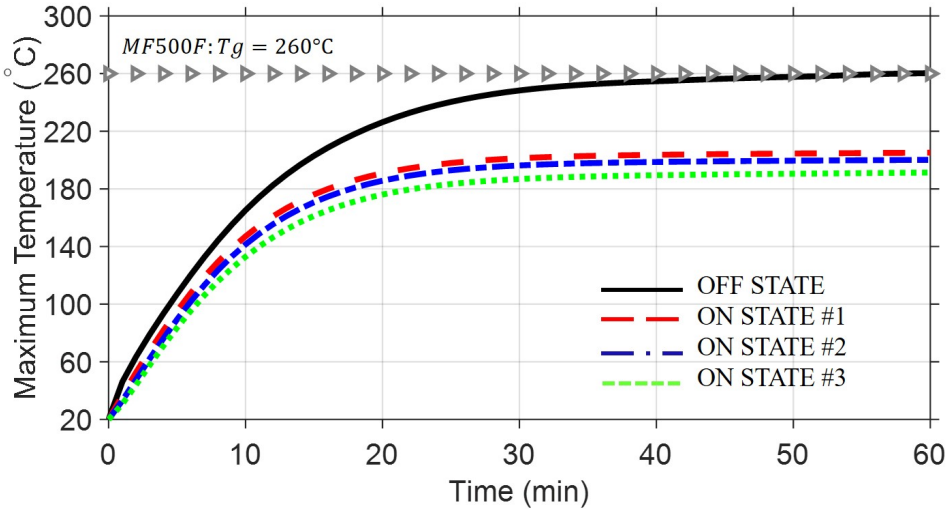

Figure 5.8: Time variant simulated peak temperature plot at different plasma states throughout the MF500F-112 substrates when exposed to S_A =10 kW/m^2 power density with incident plane EM wave at their specific absorption center frequency.

that higher absorption is mainly due to the magneto-dielectrics. As predicted, for different tuning states of the plasma at their specific center frequency, the volume loss density value has proportionally decreased with the increase of the plasma frequency. We further investigate the transient state thermal analysis of the multilayer absorber exposed to the tolerated incident power density obtained previously at OFF state (S_A =10 kW/m^2) for all the tuning states of the plasma described in Table 5.4. Simulated results (see Figure 5.8 predict that lower temperatures are generated within the the MF500F-112 substrates at ON state cases with respect to the OFF state case. Based on this study, the incident power density S_A =10 kW/m^2 is in fact the average maximum power handling capability of the design for all plasma states.

5.2 Experimental results of the temperature distribution on the top surface of the absorber

Testing the power handling capability of specific microwave components requires technical safety measures. All the test instruments have to be rated for the measurement environment and safety practices recommended by IEEE standards on high power testing should be adopted. The test setup can differ given the specific DUT. For example, when testing the power handling of a microwave filter, the input of the DUT can be driven with a coax connection and the output terminated using a high power load. Radiated susceptibility measurement of antennas are often performed in a semi-anechoic chamber. Nevertheless, all these test procedures require the use of a high power microwave source.

To validate the thermal numerical results of the multilayer tunable plasma-based absorber, a 40 dB traveling wave tube (TWT) amplifier from Hughes (Model #: 1177H13F000) operating in the S/C-band (3 GHz to 8 GHz) is used to generate a high power microwave. Since the power handling limit of the absorber is associated with the thermal effect, the temperature of the absorbing material under RF fields is measured using a thermal imaging infrared camera (FLIR E6). This IR camera has the capability to detect object temperatures ranging from −20 °C to 250 °C with 2% reading accuracy. As a safety precaution, the thermal analysis tests are performed with relatively moderate far field power densities. Although the incident power level might not test the design to its limits, it is sufficient enough to cause heat generation that can be measured using the IR camera. An illustrative sketch of the test setup is shown in Figure 5.9(a). Prior to the experiment, a sinusoidal wave produced by Keysight's E8257D PSG RF analog signal generator (2500 kHz to 20 GHz) is amplified by the TWT power amplifier and the output is monitored using the E4418B EPM series power meter. Thus, by placing the DUT at the far-field (0.5 m) from the PE9887-11

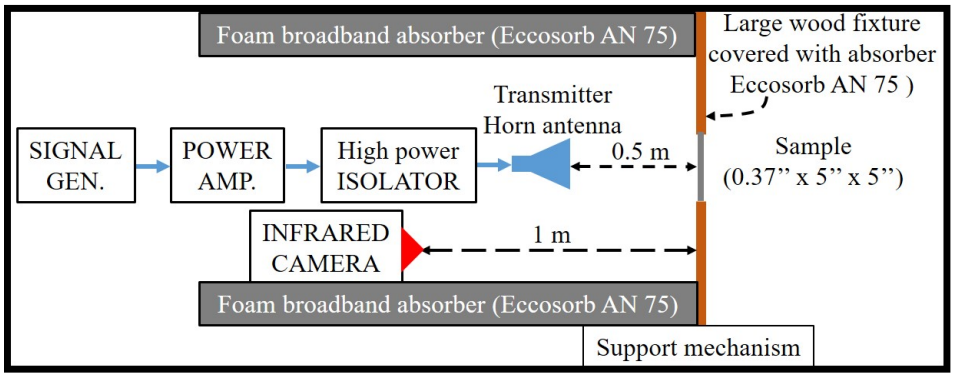

(a)

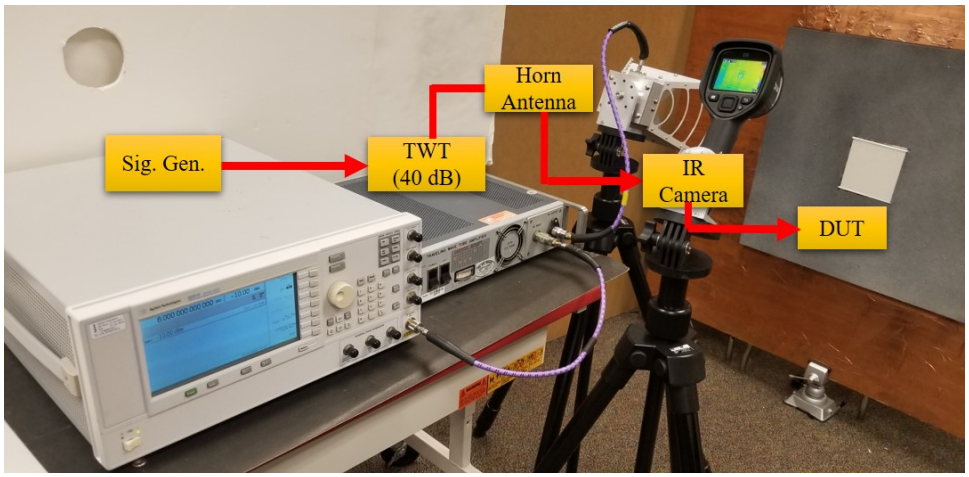

(b)

Figure 5.9: (a) Sketch and (b) photograph of the free space test setup.

broadband horn antenna, the incident power density is evaluated using the equation:

$$S = \frac{P_t G_t}{4\pi R^2} \tag{5.2}$$

where P_t is the transmitted power, $G_t = 12.6$ is the gain of the transmit horn antenna, and R is the distance from the horn antenna to the center of the top surface of the DUT. The measured thermal distribution is obtained at two different power densities ($S = 0.2$ and $0.3\,\mathrm{kW/m^2}$). A photograph of the test measurement is shown in Figure 5.9(b). Since only the top surface of the absorber is visible to the FLIR E6 IR camera, the temperature

distribution on the top surface of the absorber is measured and compared to the numerical results. The numerical analysis of the thermal transient state of the absorber upon an incident RF power density at 6 GHz is performed.

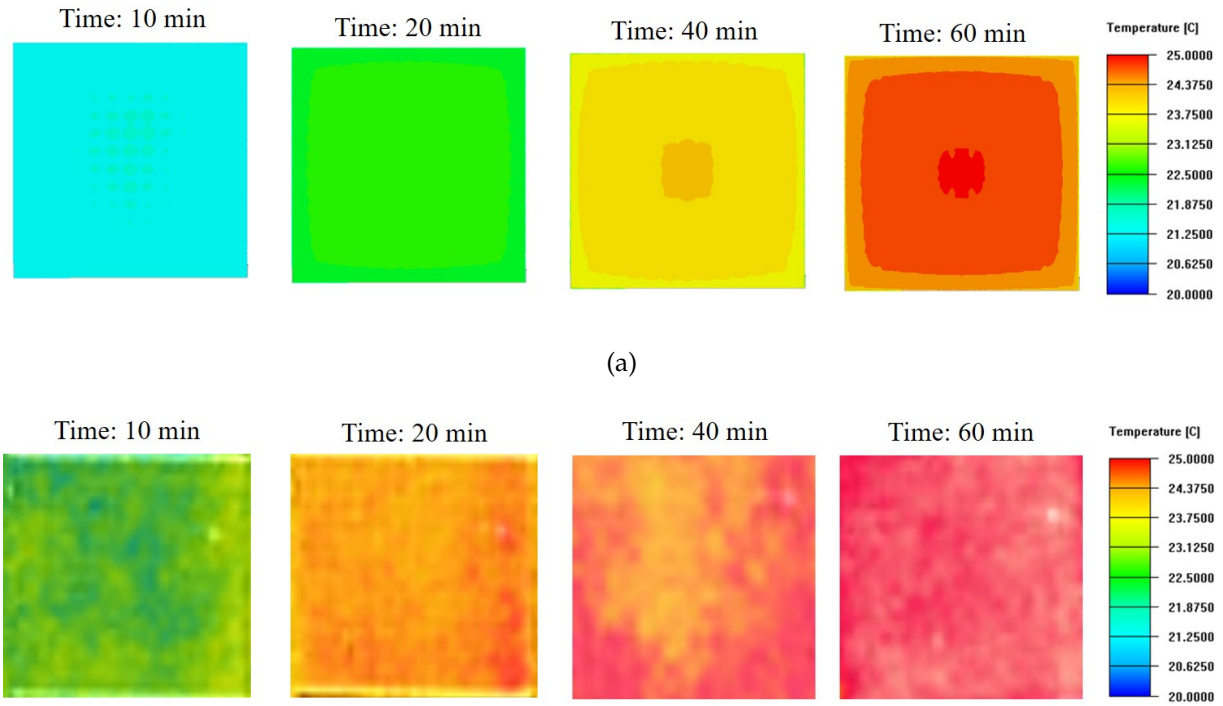

Figure 5.10: (a) Transient state temperature map observed at the top surface of the multilayer absorber (at OFF state) exposed to a power density power S =0.2 kW/m^2. (a) Simulated results for incident plane EM wave at f_0 = 6.0 GHz; (b) Measured results for incident plane EM wave at f_0 = 6.1 GHz.

The simulated temperature distributions obtained on the top surface of the absorber at OFF state are shown in Figure 5.10(a). In order to accurately measure the radiated temperature on top of the absorber, the IR camera is properly calibrated, the emissivity is set to 0.9 and the distance between the object and camera is set to 1 m. Images obtained from the IR camera are depicted in Figure 5.10(b). It shows that the top surface of the absorber becomes hotter for different time frames. The qualitative aspect of the simulated tempera-

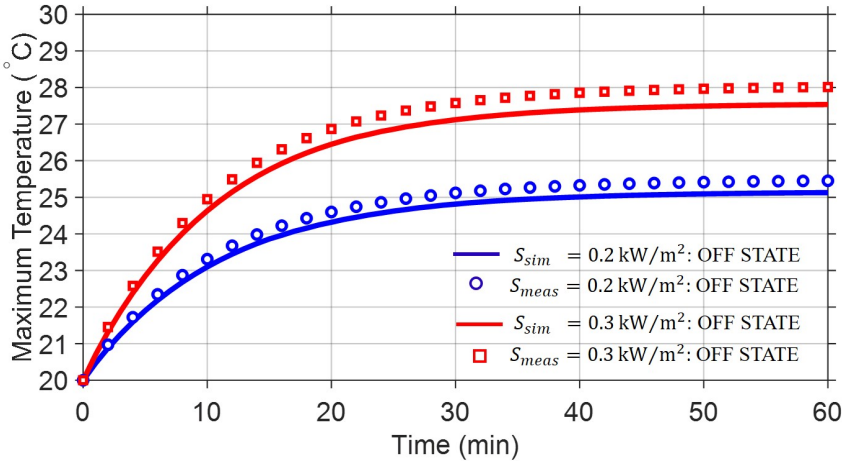

Figure 5.11: Simulated/Measured time variant temperature plots obtained at the center of the top surface of the absorber at OFF state versus time illustrated for various power densities with incident plane EM wave.

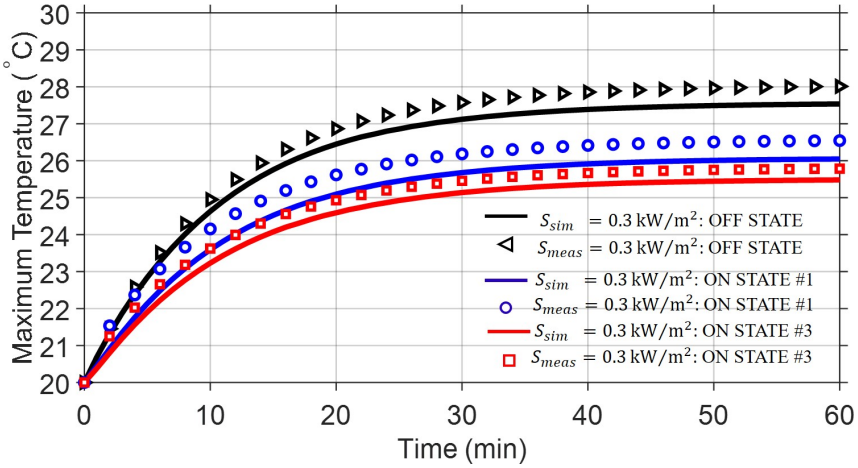

Figure 5.12: Simulated/Measured time variant temperature plots obtained at the center of the top surface of the absorber at OFF state versus time illustrated for various plasma state when the incident power densities is set to 0.3 kW/m^2.

ture profile does not exactly correspond to the measured temperature map obtained of the top surface of the multilayer absorber. Several parameters such as the color visualization used in the simulation of the design model, the lighting in the test room, the air flow in the room or the position of the IR camera surely influence the results. However, the measured temperature obtained at the center of the top surface of the multilayer absorber accurately

validates its numerical counterpart as observed in Figure 5.11 for various incident power densities. Furthermore, by fixing the incident power density to $0.3\,\mathrm{kW/m^2}$, the transient measured temperature at the center of the top surface is obtained for different tuning states of the plasma (described in Table 5.4). The measured results agree well with their numerical counterpart results shown in Figure 5.12.

6. Summary of Research

In this project, a low-profile tunable absorber based on lossy FSS layers embedded with discrete plasma-shells is investigated. The bulk plasma is modeled using a parallel plate topology and a transmission line approach is provided to explain the working principle of the proposed plasma-based tunable absorbers. Through full wave electromagnetic simulation, it is demonstrated that by adjusting the plasma frequency of the gas volume, a tuning of the absorption band is achieved. A prototype of the large-scale plasma-based absorber is fabricated and tested. The biasing voltage used to sustain the plasma is properly adjusted to control the transfer function of the absorber to validate the tunability capability that was expected from the simulation results.

Furthermore, by leaning toward applications requiring protection from high power HPM/EMP emanated by frequency agile microwave weapons or radar systems, we introduced a compact multilayer tunable absorber based on lossy magneto-dielectric substrates embedded with discrete plasma-shells. The discrete plasma-shells located on different layers of the structure allow independent control of each resonant frequency. The techniques employed in the proposed design lend much freedom to customize both functional and physical characteristics of the absorber. This thickness customizable compact multilayer absorber is tuned in real time to provide a multifunctional response on demand for a dynamic use of the EM spectrum. The power handling capability of our proposed multilayer absorber is studied. Notably, we investigate the physical effect of high peak and average power, which can present severe challenges in a harsh electromagnetic environment. A coupled physical phenomena between both RF and thermal simulation provides rigorous multiphysics simulated results, thus predicts very well the thermal issues for high-power applications. High power analysis of microwave components is very crucial in a sense that

selected materials can be rightfully chosen in the early stages of design in order to avoid failure of the final product for specific applications and assure a safe operating in harsh environments. Per se, multiphysics analysis can result in optimized design techniques to reduce susceptibility of microwave components to fail under high power excitation. In [74], optimization techniques have been investigated to mitigate field enhancement in resonant structures. The widening of capacitive gaps between metallic patches, filleting of sharp metallic corners, and the use of genetic algorithms (pixelized screen geometry) have reduced the MFEF of such designs. In addition, by substituting capacitive metallic layers with high permittivity thin dielectric, the MFEF value can be further reduced [72]. In the case of thermal management, custom design techniques such as the use of hollow pyramidal and honeycomb lossy materials, integration of a cooling system within the design, and the use of high temperature materials can increase the power handling capability.

The outcomes of our research will lead to a new class of reconfigurable, high performance, high-order spatial filters and absorbers for stable communication links from high power interference. While this research was only applicable to planar EM structures, future research can explore the versatility of the proposed technique on conformal multilayered reconfigurable FSSs/absorbers to validate the usability and the effect of incorporating inverter layers under non-planar structural formations. Also, given high demand for broadband and high data rate communication, plasma-based reconfigurable structures will be investigated over a wide range of spectrum from millimeter wave, terahertz (THz), up to optical frequencies. This forthcoming research will present certain degree of theoretical and experimental challenges due to the micro-scale design features.

7. List of publications for the project

7.1 Published

a K. Payne, J. K. Lee, K. Xu, and J. H. Choi, "Compact third-order bandpass frequency selective surface with wide spurious-suppression bandwidth," in *2018 IEEE International Symposium on Antennas and Propagation USNC/URSI National Radio Science Meeting*, pp. 2037–2038, July 2018

b K. Payne, K. Xu, J. H. Choi, and J. K. Lee, "Plasma-enabled adaptive absorber for high-power microwave applications," *IEEE Transactions on Plasma Science*, vol. 46, pp. 934–942, April 2018

c K. Payne, J. K. Lee, K. Xu, and J. H. Choi, "Low-profile plasma-based tunable absorber," in *2018 IEEE International Symposium on Antennas and Propagation USNC/URSI National Radio Science Meeting*, pp. 2065–2066, July 2018

d K. Payne, K. Xu, and J. H. Choi, "Generalized synthesized technique for the design of thickness customizable high-order bandpass frequency-selective surface," *IEEE Transactions on Microwave Theory and Techniques*, vol. 66, pp. 4783–4793, Nov 2018

e K. Payne, K. Xu, J. H. Choi, and J. K. Lee, "Electrically tunable microwave absorber based on discrete plasma-shells," *IEEE Transactions on Antennas and Propagation*, vol. 67, pp. 6523–6531, October 2019

f K. Payne, J. K. Lee, K. Xu, and J. H. Choi, "Higher order plasma-based tunable absorber using magneto-dielectric substrates," in *2019 IEEE International Symposium on Antennas and Propagation and USNC-URSI Radio Science Meeting*, pp. 2027–2028,

July 2019

7.2 Submitted

a K. Payne, K. Xu, J. H. Choi, and J. K. Lee, “Multiphysics analysis of plasma-based tunable absorber for high power microwave applications”, IEEE Transactions on Antennas and Propagation, 2020 (in review).

Bibliography

[1] C. A. Robinson, "Radar counters camouflage," *Signal*, June 2007.

[2] D. MacDonald, J. Isenman, and J. Roman, "Radar detection of hidden targets," in *Proceedings of the IEEE 1997 National Aerospace and Electronics Conference*, vol. 2, pp. 846–855, July 1997.

[3] W. F. Bahret, "The beginnings of stealth technology," *IEEE Transactions on Aerospace and Electronic Systems*, vol. 29, pp. 1377–1385, Oct. 1993.

[4] M. Skolnik, *Radar Handbook, 2nd ed.* New York, NY, USA: McGraw-Hill, 1990.

[5] R. L. Fante and M. T. McCormack, "Reflection properties of the Salisbury screen," *IEEE Transactions on Antennas and Propagation*, vol. 36, pp. 1443–1454, Oct. 1988.

[6] L. J. Du Toit, "The design of Jauman absorbers," *IEEE Antennas and Propagation Magazine*, vol. 36, pp. 17–25, Dec 1994.

[7] W. Dallenbach and W. Kleinsteuber, "Reflection and absorption of decimetre-waves by plane dielectric layers," *Hochfreq. U Elektroak*, vol. 51, no. 12, pp. 152–156, 1938.

[8] B. A. Munk, *Frequency selective surfaces: Theory and Design*. New York, NY, USA:: Wiley, 2000.

[9] Y. Shang, Z. Shen, and S. Xiao, "On the design of single-layer circuit analog absorber using double-square-loop array," *IEEE Transactions on Antennas and Propagation*, vol. 61, pp. 6022–6029, Dec. 2013.

[10] N. Engheta, "Thin absorbing screens using metamaterial surfaces," in *IEEE Antennas*

and Propagation Society International Symposium (IEEE Cat. No.02CH37313), vol. 2, pp. 392–395, Jun. 2002.

[11] F. Costa, A. Monorchio, and G. Manara, "Analysis and design of ultra thin electromagnetic absorbers comprising resistively loaded high impedance surfaces," *IEEE Transactions on Antennas and Propagation*, vol. 58, pp. 1551–1558, May 2010.

[12] A. Kazem Zadeh and A. Karlsson, "Capacitive circuit method for fast and efficient design of wideband radar absorbers," *IEEE Transactions on Antennas and Propagation*, vol. 57, pp. 2307–2314, Aug. 2009.

[13] W. Tang, G. Goussetis, H. Legay, and N. J. G. Fonseca, "Efficient synthesis of low-profile angularly-stable and polarization-independent frequency-selective absorbers with a reflection band," *IEEE Transactions on Antennas and Propagation*, vol. 63, pp. 621–629, Feb 2015.

[14] A. R. Hunt, "Use of a frequency-hopping radar for imaging and motion detection through walls," *IEEE Transactions on Geoscience and Remote Sensing*, vol. 47, pp. 1402–1408, May 2009.

[15] M. Jankiraman, *Design of multi-frequency CW radars*. Raleigh, NC, USA:: SciTech, 2007.

[16] A. Tennant and B. Chambers, "A single-layer tuneable microwave absorber using an active FSS," *IEEE Microwave and Wireless Components Letters*, vol. 14, pp. 46–47, Jan. 2004.

[17] J. Zhao, Q. Cheng, J. Chen, M. Q. Qi, W. X. Jiang, and T. J. Cui, "A tunable metamaterial absorber using varactor diodes," *New Journal of Physics*, vol. 15, p. 43049, apr 2013.

[18] T. Nesimoglu and C. Sabah, "A frequency tunable metamaterial resonator using

varactor diodes," in *2016 16th Mediterranean Microwave Symposium (MMS)*, pp. 1–4, Nov. 2016.

[19] C. Mias and J. H. Yap, "A varactor-tunable high impedance surface with a resistive-lumped-element biasing grid," *IEEE Transactions on Antennas and Propagation*, vol. 55, pp. 1955–1962, Jul. 2007.

[20] F. Hu, Y. Qian, Z. Li, J. Niu, K. Nie, X. Xiong, W. Zhang, and Z. Peng, "Design of a tunable terahertz narrowband metamaterial absorber based on an electrostatically actuated MEMS cantilever and split ring resonator array," *Journal of Optics*, vol. 15, p. 55101, Mar. 2013.

[21] V. Fusco, R. Cahill, W. Hu, and S. Simms, "Ultra-thin tunable microwave absorber using liquid crystals," *Electronics Letters*, vol. 44, pp. 37–38, Jan. 2008.

[22] D. Shrekenhamer, W.-C. Chen, and W. J. Padilla, "Liquid crystal tunable metamaterial absorber," *Phys. Rev. Lett.*, vol. 110, p. 177403, Apr. 2013.

[23] Y. Zhang, Y. Feng, B. Zhu, J. Zhao, and T. Jiang, "Graphene based tunable metamaterial absorber and polarization modulation in terahertz frequency," *Opt. Express*, vol. 22, pp. 22743–22752, Sep. 2014.

[24] B. Xu, C. Gu, Z. Li, L. Liu, and Z. Niu, "A novel absorber with tunable bandwidth based on graphene," *IEEE Antennas and Wireless Propagation Letters*, vol. 13, pp. 822–825, May 2014.

[25] Q. H. Song, W. Zhu, P. Wu, W. Zhang, Q. Wu, J. Teng, Z. Shen, P. Chong, Q. Liang, Z. Yang, *et al.*, "Liquid-metal-based metasurface for terahertz absorption material: Frequency-agile and wide-angle," *APL Materials*, vol. 5, no. 6, p. 066103, 2017.

[26] D. Paiva, M. Silva, T. Ribeiro, I. Vasconcelos, A. Sombra, J. Góes, and P. Fechine, "Novel magnetic–dielectric composite ceramic obtained from y3fe5o12 and catio3," *Journal of Alloys and Compounds*, vol. 644, pp. 763–769, 2015.

[27] R. E. Diaz, M. C. Miller, M. M. L. Re, J. P. Gilb, and S. Alam, "Synthetic magnetodielectric with controlled off-normal te and tm response," Sept. 12 2000. US Patent 6,117,517.

[28] M. Jafarian, S. S. S. Afghahi, Y. Atassi, and A. Sabzi, "New insights on microwave absorption characteristics of magnetodielectric powders: effect of matrix chemical nature and loading percentage," *Journal of Magnetism and Magnetic Materials*, vol. 492, p. 165624, 2019.

[29] J. H. Choi, J. S. Sun, and T. Itoh, "An alternative technique in designing a low-profile two-pole bandpass frequency selective surface (FSS) using aperture coupling interlayer," in *2013 IEEE MTT-S International Microwave Symposium Digest (MTT)*, pp. 1–3, June 2013.

[30] K. Payne and J. H. Choi, "Third-order frequency selective surface based on inverter interlayers," in *2016 IEEE International Symposium on Antennas and Propagation (APSURSI)*, pp. 953–954, June 2016.

[31] K. Payne, K. Xu, and J. H. Choi, "Generalized synthesized technique for the design of thickness customizable high-order bandpass frequency-selective surface," *IEEE Transactions on Microwave Theory and Techniques*, vol. 66, pp. 4783–4793, Nov 2018.

[32] R. J. Vidmar, "On the use of atmospheric pressure plasmas as electromagnetic reflectors and absorbers," *IEEE Transactions on Plasma Science*, vol. 18, pp. 733–741, Aug 1990.

[33] J. P. Rybak, "Causes, effects and diagnostic measurements of the reentry plasma sheath," tech. rep., Colorado State Univ. Fort Collins, Dept. of Electrical Engineering, Fort Collins, CO, USA, Dec 1970.

[34] G. Yang, J.-C. Tan, D.-Y. Sheng, and Y.-C. Yang, "Plasma limiter for protecting against high power microwave," *J. Sci. Ind. Res.*, vol. 67, pp. 685—687, Sep. 2008.

[35] W. Destler, J. DeGrange, H. Fleischmann, J. Rodgers, and Z. Segalov, "Experimental studies of high-power microwave reflection, transmission, and absorption from a plasma-covered plane conducting boundary," *Journal of applied physics*, vol. 69, pp. 6313–6318, May 1991.

[36] J. C. Vardaxoglou, "Optical switching of frequency selective surface bandpass response," *Electronics Letters*, vol. 32, pp. 2345–2346, Dec 1996.

[37] T. Anderson, I. Alexeff, J. Raynolds, E. Farshi, S. Parameswaran, E. P. Pradeep, and J. Hulloli, "Plasma frequency selective surfaces," *IEEE Transactions on Plasma Science*, vol. 35, pp. 407–415, April 2007.

[38] L. W. Cross, C. A. Wedding, D. K. Wedding, and E. F. Peter, "Frequency selective surfaces." U.S. Patent 0 098 893 A1, April 2017.

[39] K. Payne, E. F. Peters, J. Brunett, D. K. Wedding, C. A. Wedding, and J. H. Choi, "Second-order plasma enabled tunable low-profile frequency selective surface based on coupling inter-layer," in *2016 46th European Microwave Conference (EuMC)*, pp. 309–312, Oct 2016.

[40] K. Payne, J. H. Choi, E. Peters, D. Wedding, and C. Wedding, "Plasma-tunable electronic protection for microwave applications," in *2017 IEEE International Symposium*

on Antennas and Propagation USNC/URSI National Radio Science Meeting, pp. 259–260, July 2017.

[41] M. A. Lieberman and A. J. Lichtenberg, *Principles of Plasma Discharges and Materials Processing*. Hoboken, NJ, USA: Wiley, 2005.

[42] Y. Itikawa, "Effective collision frequency of electrons in gases," *The Physics of Fluids*, vol. 16, pp. 831–835, June 1973.

[43] L. W. Cross, M. J. Almalkawi, and V. K. Devabhaktuni, "Development of large-area switchable plasma device for x-band applications," *IEEE Transactions on Plasma Science*, vol. 41, pp. 948–954, April 2013.

[44] O. Luukkonen, C. Simovski, G. Granet, G. Goussetis, D. Lioubtchenko, A. V. Raisanen, and S. A. Tretyakov, "Simple and accurate analytical model of planar grids and high-impedance surfaces comprising metal strips or patches," *IEEE Transactions on Antennas and Propagation*, vol. 56, pp. 1624–1632, June 2008.

[45] K. N. Rozanov, "Ultimate thickness to bandwidth ratio of radar absorbers," *IEEE Transactions on Antennas and Propagation*, vol. 48, pp. 1230–1234, Aug 2000.

[46] P. Baille, J. S. Chang, A. Claude, R. M. Hobson, G. L. Ogram, and A. W. Yau, "Effective collision frequency of electrons in noble gases," *Journal of Physics B: Atomic and Molecular Physics*, vol. 14, pp. 1485–1495, May 1981.

[47] X.-M. Zhu, W.-C. Chen, S. Zhang, Z.-G. Guo, D.-W. Hu, and Y.-K. Pu, "Electron density and ion energy dependence on driving frequency in capacitively coupled argon plasmas," *Journal of Physics D: Applied Physics*, vol. 40, pp. 7019–7023, nov 2007.

[48] V. A. Godyak, *Soviet Radio Frequency Discharge Research*. Falls Church, VA: Delphic Associates, 1986.

[49] Y. Patenaude, T. E. Durham, J. D. Struttmann, R. C. Taylor, A. Zaricki, W. R. Whaley, and J. A. Kralovec, "Dual band hybrid solid/dichroic antenna reflector." U.S. Patent 6 140 978, October 2000.

[50] K. Payne, K. Xu, J. H. Choi, and J. K. Lee, "Electrically tunable microwave absorber based on discrete plasma-shells," *IEEE Transactions on Antennas and Propagation*, vol. 67, pp. 6523–6531, October 2019.

[51] X. Sun, M. Cheng, S. Zhu, and J. Zhang, "Coupled electromagnetic-thermal-mechanical analysis for accurate prediction of dual-mechanical-port machine performance," *IEEE Transactions on Industry Applications*, vol. 48, pp. 2240–2248, Nov 2012.

[52] J. Jin and S. Yan, "Multiphysics modeling in electromagnetics: Technical challenges and potential solutions," *IEEE Antennas and Propagation Magazine*, vol. 61, pp. 14–26, April 2019.

[53] D. C. Schleher, *Introduction to electronic warfare*. Dedham, MA, Artech House, 1986.

[54] A. E. Spezio, "Electronic warfare systems," *IEEE Transactions on Microwave Theory and Techniques*, vol. 50, pp. 633–644, March 2002.

[55] D. C. Schleher, *Electronic warfare in the information age*. Artech House, Inc., 1999.

[56] G. H. Sung, K. W. Sowerby, M. J. Neve, and A. G. Williamson, "A frequency-selective wall for interference reduction in wireless indoor environments," *IEEE Antennas and Propagation Magazine*, vol. 48, pp. 29–37, Oct 2006.

[57] S. Scott, C. D. Nordquist, J. Custer, D. Leonhardt, T. S. Jordan, and C. T. Rodenbeck, "Band-selective interferer rejection for cognitive receiver protection," in *2013 IEEE MTT-S International Microwave Symposium Digest (MTT)*, pp. 1–4, June 2013.

[58] L. W. Cross, M. J. Almalkawi, and V. K. Devabhaktuni, "Theory and demonstration of narrowband bent hairpin filters integrated with ac-coupled plasma limiter elements," *IEEE Transactions on Electromagnetic Compatibility*, vol. 55, pp. 1100–1106, Dec 2013.

[59] E. Rocas, A. Padilla, J. Mateu, N. Orloff, J. M. O'Callaghan, C. Collado, and J. C. Booth, "Superconducting multiplexer filter bank for a frequency-selective power limiter," *IEEE Transactions on Applied Superconductivity*, vol. 21, pp. 542–546, June 2011.

[60] P. Phudpong and I. C. Hunter, "Frequency-selective limiters using nonlinear bandstop filters," *IEEE Transactions on Microwave Theory and Techniques*, vol. 57, pp. 157–164, Jan 2009.

[61] K. Payne, K. Xu, J. H. Choi, and J. K. Lee, "Plasma-enabled adaptive absorber for high-power microwave applications," *IEEE Transactions on Plasma Science*, vol. 46, pp. 934–942, April 2018.

[62] S. Sciancalepore and R. Di Pietro, "Bittransfer: Mitigating reactive jamming in electronic warfare scenarios," *IEEE Access*, vol. 7, pp. 156175–156190, 2019.

[63] B. Bai, Y. Liu, L. Song, X. Li, Y. Ding, and X. Zhang, "Passive radar jamming: A novel method using time-varying plasma," *IEEE Access*, vol. 7, pp. 120082–120088, 2019.

[64] E. Al-Shaer, J. Wei, K. W. Hamlen, and C. Wang, "Deception-enhanced threat sensing for resilient intrusion detection," in *Autonomous Cyber Deception*, pp. 147–165, Springer, 2019.

[65] C. E. Baum, "From the electromagnetic pulse to high-power electromagnetics," *Proceedings of the IEEE*, vol. 80, no. 6, pp. 789–817, 1992.

[66] S.-H. Min, O. Kwon, M. Sattorov, H. Jung, I.-K. Baek, S. Kim, J.-Y. Jeong, J. Jang, D. Hong, R. Bhattacharya, R. K. Barik, A. Bera, S. Park, J. Ahn, S. H. Lee, Y. J. Yoon,

and G.-S. Park, "Effects on electronics exposed to high-power microwaves on the basis of a relativistic backward-wave oscillator operating on the x-band," *Journal of Electromagnetic Waves and Applications*, vol. 31, no. 17, pp. 1875–1901, 2017.

[67] E. Van Keuren and J. Knighten, "Implications of the high-power microwave weapon threat in electronic system design," in *IEEE 1991 International Symposium on Electromagnetic Compatibility*, pp. 370–371, July 1991.

[68] C. Wilson, "High altitude electromagnetic pulse (hemp) and high power microwave (hpm) devices: Threat assessments," in *LIBRARY OF CONGRESS WASHINGTON DC*, CONGRESSIONAL RESEARCH SERVICE, 2008.

[69] A. A. Neuber, G. F. Edmiston, J. T. Krile, H. Krompholz, J. C. Dickens, and M. Kristiansen, "Interface breakdown during high-power microwave transmission," *IEEE Transactions on Magnetics*, vol. 43, pp. 496–500, Jan 2007.

[70] C. M. Sabliov, D. A. Salvi, and D. Boldor, "High frequency electromagnetism, heat transfer and fluid flow coupling in ANSYS multiphysics," *Journal of Microwave Power and Electromagnetic Energy*, vol. 41, no. 4, pp. 5–17, 2006.

[71] D. Salvi, D. Boldor, J. Ortego, G. M. Aita, and C. M. Sabliov, "Numerical modeling of continuous flow microwave heating: A critical comparison of COMSOL and ANSYS," *Journal of Microwave Power and Electromagnetic Energy*, vol. 44, no. 4, pp. 187–197, 2010.

[72] M. Li and N. Behdad, "Frequency selective surfaces for pulsed high-power microwave applications," *IEEE Transactions on Antennas and Propagation*, vol. 61, pp. 677–687, Feb 2013.

[73] D. Fitzpatrick, "Chapter 15 - temperature analysis," in *Analog Design and Simulation Using OrCAD Capture and PSpice (Second Edition)*, pp. 209 – 216, Newnes, 2018.

[74] J. A. Bossard, C. P. Scarborough, Q. Wu, S. D. Campbell, D. H. Werner, P. L. Werner, S. Griffiths, and M. Ketner, "Mitigating field enhancement in metasurfaces and metamaterials for high-power microwave applications," *IEEE Transactions on Antennas and Propagation*, vol. 64, pp. 5309–5319, Dec 2016.

[75] K. Payne, J. K. Lee, K. Xu, and J. H. Choi, "Compact third-order bandpass frequency selective surface with wide spurious-suppression bandwidth," in *2018 IEEE International Symposium on Antennas and Propagation USNC/URSI National Radio Science Meeting*, pp. 2037–2038, July 2018.

[76] K. Payne, J. K. Lee, K. Xu, and J. H. Choi, "Low-profile plasma-based tunable absorber," in *2018 IEEE International Symposium on Antennas and Propagation USNC/URSI National Radio Science Meeting*, pp. 2065–2066, July 2018.

[77] K. Payne, J. K. Lee, K. Xu, and J. H. Choi, "Higher order plasma-based tunable absorber using magneto-dielectric substrates," in *2019 IEEE International Symposium on Antennas and Propagation and USNC-URSI Radio Science Meeting*, pp. 2027–2028, July 2019.